A COMPUTATIONAL STUDY ON THE UNSTEADY SHOCK WAVE DYNAMICS AROUND A CIRCULAR ARC AIRFOIL IN TRANSONIC INTERNAL FLOW

by

Md. Mostaqur Rahman

A thesis

Submitted to the

Department of Mechanical Engineering

in partial fulfillment of the requirements for the degree

of

MASTER OF SCIENCE IN MECHANICAL ENGINEERING

BANGLADESH UNIVERSITY OF ENGINEERING AND TECHNOLOGY,

DHAKA-1000, BANGLADESH

FEBRUARY 2013

The thesis titled "**A Computational Study on the Unsteady Shock Wave Dynamics around a Circular Arc Airfoil in Transonic Internal Flow"** submitted by **Md. Mostaqur Rahman,** Roll No. 1009102034P, Session October 2009 has been accepted satisfactory in partial fulfillment for the degree of Master of Science in Mechanical Engineering on February 14, 2013

BOARD OF EXAMINERS

_____

Dr. A. B. M. Toufique Hasan — Chairman
Assistant Professor
Department of Mechanical Engineering
BUET, Dhaka-1000

_____

Prof. Dr. Md. Ehsan — Member (Ex-Officio)
Head
Department of Mechanical Engineering
BUET, Dhaka-1000

_____

Dr. Mohammad Mamun — Member
Associate Professor
Department of Mechanical Engineering
BUET, Dhaka-1000

_____

Dr. Md. Mahbubul Alam — Member (External)
Professor
Department of Mechanical Engineering
Chittagong University of Engineering & Technology (CUET)
Chittagong-4349

CANDIDATE'S DECLARATION

It is hereby declared that this thesis or any part of it has not been submitted elsewhere for the award of any degree or diploma.

_____

Md. Mostaqur Rahman

Student ID: 1009102034

ACKNOWLEDGEMENT

The author would like to express his deep gratitude and indebtedness to his supervisor Dr. A. B. M. Toufique Hasan, Assistant Professor, Department of Mechanical Engineering, Bangladesh University of Engineering & Technology (BUET), for his continuous inspiration, great interest, constructive criticism, super guidance, remarkable advice and invaluable support during this research. The author would also like to thank him for his careful reading and correction of this thesis.

The author also wants to express his gratitude to the Head, Department of Mechanical Engineering, BUET, for his cooperation and help to continue this research work.

Very special thanks are due for all teachers of the Department of Mechanical Engineering, BUET for their help to the author during the whole period of his M. Sc. Engineering courses.

Finally, the author expresses his gratefulness to DUET authority for allowing him to complete this research program granting him leave and necessary permissions.

NOMENCLATURE

ρ = Density of Air

t = Time

C_p = Pressure Coefficient

x = Airfoil chord distance from leading edge

c = Chord length of the airfoil

f = Frequency of oscillation

μ = Absolute viscosity of air

p = Total outlet pressure

p_{in} = Inlet pressure

p_{rms} = Root Mean Square of pressure

M_∞ = Free Stream Mach number

v_∞ = Free Stream velocity of air

Re = Reynolds number

T_∞ = Ambient temperature

k = Turbulent kinetic energy

ω = Specific dissipation rate

PR = Pressure Ratio (p/p_{in})

TABLE OF CONTENTS

LIST OF FIGURES

FIGURES **PAGE**

FIGURES **PAGE**

FIGURES **PAGE**

LIST OF TABLES

TABLES **PAGE**

ABSTRACT

Self-sustained shock wave oscillations on airfoils at transonic flow conditions are associated with the phenomenon of buffeting. The physical mechanisms of the periodic shock motion are not yet fully understood even though experiments performed over fifty years ago have demonstrated the presence of oscillatory shock waves on the airfoil surfaces at high subsonic speeds. The unsteady pressure fluctuations generated by the low-frequency large-amplitude shock motions are highly undesirable from the structural integrity and aircraft maneuverability point of view. Dynamics of unsteady shock wave phenomena around a biconvex circular arc airfoil in transonic internal flow fields are often observed due to complex shock wave boundary layer interaction. Numerical model is developed to predict the self-excited shock oscillation around a biconvex circular arc airfoil in transonic internal flow. A commercial finite volume CFD package has been used for this computation. The computational domain has been discretized into a structured mesh by using a commercial preprocessing tool. The transonic flow around a biconvex airfoil is governed by the unsteady compressible Reynolds-average Navier-Stokes equation together with the energy equation. Two additional equations of κ-ω SST turbulence model have been included to model the turbulence in the flow field. Unsteady shock wave phenomena numerically studied for outlet pressure to inlet pressure ratios of 0.71–0.75. The characteristics of self-excited shock wave dynamics under various flow conditions such as total pressure ratio, free stream Mach number and so on were investigated and then used to classify the types of shock wave. The results obtained from the numerical computation have been validated with the experimental results. The various modes of shock wave motion for different flow conditions are described. The mechanisms of self-sustained shock oscillations are discussed for symmetrical circular-arc airfoils at zero incidence angles. Finally, cavity method has been used to control the shock oscillation and find its effectiveness.

CHAPTER 1

INTRODUCTION

1.1 Motivation for Research

At transonic flow conditions, unsteady shock waves are frequently observed in several modern internal aeronautical applications such as in turbine cascades, compressor blades, butterfly valves, fans, nozzles, diffusers and so on. In these cases, the interaction of shock waves with the boundary layers becomes complex and generates unsteady self-excited shock induced oscillation (SIO) in the flow fields [1-5]. Aeroacoustic noise, nonsynchronous vibration (NSV), intense drag rise, high cycle fatigue failure (HCF), buffeting and so on are the detrimental consequences of this shock oscillation.

The self-excited oscillation around an airfoil caused by the interaction of large-scale flow separation and shock wave was studied by several researchers [6-8]. Large pressure fluctuation induced by the shock oscillation, acts as the periodic force, exciting the airfoil and limits the operating range. The physical mechanisms of the shock motion are not yet fully understood, because of the structures of the unsteady large separation and the unsteady shock-boundary-layer interaction. Various fundamental mechanisms involving the complex flow characteristics, such as moving shock wave behaviors, turbulent boundary layer characteristics, kinematics of coherent structures and dynamical processes in flow evolution, are still completely unclear and are of great interest for future detailed studies.

Recently, the control of the self-excited shock oscillation around an airfoil is getting intense interest. As a result, many active and passive control techniques are

being investigated. Active shock control using suction, blowing as well as zero-mass flux oscillatory blowing are introduced in aerodynamic applications. Currently, micro-blowing as a flow control technique is proposed. Beyond these, there are some promising passive control techniques which are economically more viable such as shock control bump, micro ramp and so on [9-10]. In many cases, shock oscillations can be completely suppressed or delayed to a higher Mach number or incidence angle.

1.2 Internal Transonic Flow

If the flow of a fluid is confined by a surface, it is referred to as an internal flow. Internal flows encountered in propulsion systems, fluid machinery (compressors, turbines, and pumps), ducts (diffusers, nozzles and combustion chambers) and often arise in industrial and manufacturing processes. The internal flow configuration represents a convenient geometry for heating and cooling fluids used in chemical processing, environmental control, and energy conversion technologies.

In aeronautics, transonic refers to the condition of flight in which a range of velocities of airflow exist surrounding and flowing past an air vehicle or an airfoil that are con-currently below, at, and above the speed of sound in the range of Mach 0.8 to 1.0, i.e. 600–768 mph. This condition depends not only on the travel speed of the aircraft, but also on the pressure and temperature of the airflow of the vehicle's local environment. It is formally defined as the range of speeds between the critical Mach number, when some parts of the airflow over an air vehicle or airfoil are supersonic, and at a higher speed, typically near Mach 1.2, when the vast majority of the airflow

is supersonic. Between these speeds some of the airflow is supersonic, but a significant fraction is not.

Most modern jet powered aircraft are engineered to operate at transonic air speeds. Transonic airspeeds see a rapid increase of wave drag from about Mach 0.8, and it is the fuel costs of the drag that typically limits the airspeed. Attempts to reduce wave drag can be seen on all high-speed aircraft; most notable is the use of swept wings, but another common form is a wasp-waist fuselage as a side effect of the Whitcomb area rule.

Severe instability can occur at transonic speeds. Shock waves move through the air at the speed of sound. When an object such as an aircraft also moves at the speed of sound, these shock waves build up in front of it to form a single, very large shock wave. During transonic flight, the plane must pass through this large shock wave, as well as contending with the instability caused by air moving faster than sound over parts of the wing and slower in other parts.

Transonic speeds can also occur at the tips of rotor blades of helicopters and aircraft. However, as this puts severe, unequal stresses on the rotor blade, it is avoided and may lead to dangerous accidents if it occurs. It is one of the limiting factors to the size of rotors, and also to the forward speeds of helicopters (as this speed is added to the forward-sweeping (leading) side of the rotor, thus possibly causing localized transonic flow).

The flow over an airfoil in transonic conditions is characterized in figure 1.1. Transonic flow can be divided in three sub-domains:

1. Subsonic domain

2. Sonic domain

3. Supersonic domain

Transonic phenomena occur for both subsonic and supersonic free-stream flows, because of the higher than free-stream Mach numbers on top of the (positively cambered) airfoil. From figure 1.1 it can be seen that at higher free-stream Mach numbers the subsonic domain becomes so small that it is almost none existing. The most important aspect that distinguishes transonic from both supersonic and subsonic flow is the fact that the disturbance propagation velocity and the local fluid velocity are comparable in magnitude. [33] In classical subsonic and supersonic flow theory the assumption is made that the local speed of sound is significantly higher and in the latter case significantly lower than the local velocity of the air. This allows the disturbance propagation mechanism to be uncoupled from the local flow phenomena. Transonic flow on the other hand cannot be said to be uncoupled in that manner, which implies the nonlinear coupling between the local velocity field and the propagation velocity of the perturbations have to be included in the fundamental flow equations by some additional nonlinear terms. This complicates the system considerably.

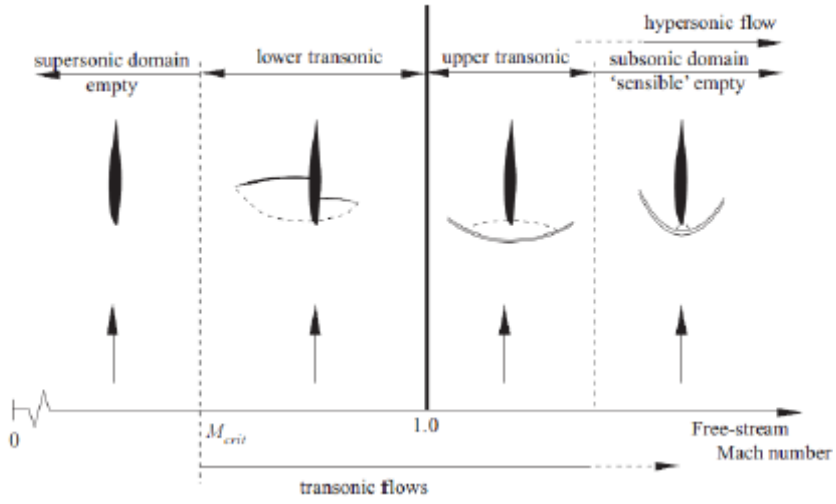

Figure 1.1: Basic classes of transonic flows

1.3 Shock Wave

A shock wave is a type of propagating disturbance. Whenever a supersonic flow abruptly changes to subsonic flow, a normal shock wave is produced. Shock waves are characterized by an abrupt, nearly discontinuous change in the characteristics of the medium. This occurs due to pressure differentials and when the Mach number of the approaching flow M>1. A shock wave is a pressure wave of finite thickness, of the order of 10^{-2} to 10^{-4} mm in the atmospheric pressure.

Shock waves are characterized by an abrupt change in the characteristics of the flow. Across a shock there is an extremely rapid rise in pressure, temperature and density of the flow. From a conservation of energy point of view one can say the total energy is conserved, total temperature and enthalpy stay the same, but the energy which can be extracted as work decreases as the entropy increases. Vorticity is generated by shock waves due to this variation of entropy across the shock. In the following sections it will become clear that this increase in entropy is one of the complicating aspects of simulating shocks in a numerical model. One could see this change in flow parameters as follows; because the pressure disturbance cannot propagate upstream in supersonic flow, the air is forced to change its properties (temperature, density, pressure, and Mach number) when in contact with a body. When this is done in a somewhat violent manner, a shock wave forms. Several different kinds of shocks can be distinguished:

(a) Normal shock: perpendicular to the air flow direction.

(b) Oblique shock: at an angle to the direction of flow.

(c) Bow shock: Occurs upstream of the front (bow) of a blunt object when the upstream velocity exceeds Mach 1.

1.4 Methodology

The aerodynamic characteristics of the present problem are solved by numerical simulation. Commercial finite volume software is used for this simulation. The computational domain is discretized into a structured mesh. The transonic flow around a circular arc airfoil is governed by the unsteady compressible Navier-Stokes equations together with the mass conservation equation and the energy equation. Two additional transport equations of k-ω SST turbulence model are included to model the turbulence in the flow field. Since the free stream Mach number of the present problem is in the range of 0.6 to 0.8, a density based solver is used. A second-order upwind scheme for the discretization of flow and turbulence equations is used. For time integration, a second order implicit scheme is used. The results obtained from the numerical simulation are validated with the available experimental results. Finally, the numerical simulation is conducted for unsteady shock wave dynamics and its control.

1.5 Objectives

The present work investigates the transonic internal flow around a 15% thick circular arc airfoil of 48 mm chord length. The key objectives of the present research are as follows,

i) To develop a numerical model to predict the self-excited shock oscillation around a biconvex circular arc airfoil in transonic internal flow.

ii) To investigate the characteristics of self-excited shock wave dynamics under various flow conditions such as total pressure ratio, free stream Mach number and so on.

iii) To determine the magnitude of frequency and amplitude of self-excited shock oscillation.

iv) To predict the suppression of self-excited shock oscillation around the airfoil using cavity.

The goal of the present research is to evaluate the cavity based passive means for the control of self-sustained shock oscillation around a biconvex airfoil through numerical computation.

CHAPTER 2

LITERATURE REVIEW

The phenomenon of unsteady self-excited shock wave oscillation has been observed experimentally and numerically by several authors investigating the transonic flow over airfoils and simple bodies in external flows. Similar phenomena can also be seen in internal flows around an airfoil such as in the flow fields of compressor blades, turbine cascades, butterfly valves, fan and so on.

H. Tijdeman [1977] had performed very detailed studies of unsteady wave phenomenon. He investigated transonic flows over oscillating airfoils and airfoils with oscillating flaps observing a periodic motion of the recompression shock. Depending on the frequency and the amplitude of the forced oscillations, in total three different types of periodic shock motions have been found. Tijdeman also observed weak pressure waves outside the boundary layer originating at the trailing edge region, propagating upstream and interacting with the shock. He proposed that a change in the flow direction at the trailing edge is the mechanism of pressure wave generation. As the flow direction at the trailing edge is connected to the circulation and lift, he called the observed waves “Kutta waves”. He further postulated that the information about the flow direction at the trailing edge is transported upstream by those “Kutta waves”.

McDevitt et al. [1976] performed an experimental and theoretical study on a thick airfoil in transonic flow. He identified Tijdeman type C SIO, with a reduced frequency of 0.49 for an 18% thick biconvex aerofoil at zero incidences over a narrow range of Mach numbers, namely: $0.73 < M < 0.78$. Small regions of Tijdeman type A SIO were also detected in the extremities of the periodic flow band. The extent of this periodic band was found to decrease considerably as the Reynolds number approached 3×10^6.

Seegmiller et al. [1978] performed an experimental investigation of the transonic flow over a 18% thick circular arc airfoil at 0-deg angle of attack at two Mach numbers, 0.76 and 0.79, and a single Reynolds number, based on chord, of $l\,l \times l0^6$.
He developed basic information for turbulence modeling of shock-induced separated flows and numerical computer codes to solve time-dependent Reynolds' averaged compressible Navier-Stokes equations. Then experimental result is verified by numerical simulation. The flow hysteresis region which McDevitt discovered was later verified by Seegmiller et al.

H. Tijdeman, R. Seebass [1980] reviewed the previous experimental results and then used to illustrate the interaction between the steady and unsteady flow fields, the periodic motion of the shock waves, and the effects of frequency and amplitude of oscillation. Further, he classified the self-excited shock induced oscillations, or SIO as being of three types, i.e. type A, B and C. Tijdeman type A SIO is where the shock wave remains distinct throughout the oscillation with a cyclic change in both the shock wave strength and location. In Tijdeman type B SIO the shock wave vanishes

for part of the cycle, normally whilst the shock is propagating upstream. Finally, Tijdeman type C SIO describes the shock wave motion whereby the shock remains distinct as it propagates upstream past the leading-edge and into the on-coming flow.

Mabey et al. [1981] detected a similar phenomenon whereby the SIO vanished within the Reynolds number range of: $3 \times 10^6 < Re < 5 \times 10^6$.

Gibb J. [1988] investigated the transonic flow around symmetric airfoils at zero incidence. He suggested that disturbances on one airfoil surface will cause wake deflections similar to a deflection of a flap. The wake asymmetry causes the Kutta wave generation at the trailing edge. The upstream moving Kutta waves change the shock position and strength in anti-phase on the upper and lower airfoil surface which results in a change in the shock–boundary layer interaction and causes boundary layer separation. He conducted a comprehensive study of flow over a 14% thick bioconvex aerofoil, detected Tijdeman type B SIO; with small regions of Tijdeman type A SIO, occurring within a narrow Mach number band.

Raghunathan et al. [1999] investigated the mechanism of the origin of shock oscillations on an 18% thick biconvex aerofoil by using a thin-layer Navier-Stokes code. Shock oscillations on an aerofoil in transonic flow were initiated by moving the aerofoil from a regime of non-periodic flow to a regime where periodic flow does occur by withdrawal of a trailing-edge splitter plate. The shock oscillations on the 18% thick biconvex aerofoil without the splitter plate appear to be type B.

Lionel L. Levy Jr. [1978] performed an experimental and computational investigation of the steady and unsteady transonic flow-fields about a thick airfoil. An operational computer code for solving the two-dimensional, compressible Navier-Stokes equations for flow over airfoils was modified to include solid-wall, slip-flow boundary conditions to properly assess the code and help guide the development of improved turbulence models. Steady and unsteady flow-fields about an 18% thick circular arc airfoil at Mach numbers of 0.720, 0.754, and 0.783 and a chord based Reynolds number of 11×10^6 are predicted and compared with experiment.

Yamamoto K., Tanida Y. [1990] investigated self-excited oscillation of transonic flow in a simplified cascade model theoretically and compared with previous experimental result then finally, a numerical simulation by the two-dimensional Navier-Strokes equation was made for qualitative understanding of the unstable flow structure of the separation region, which was not easily measured in experiment. The measurements of the shock wave and wake motions and the unsteady static pressure field predict a closed loop mechanism, in which the pressure disturbance that is generated by the oscillation of boundary layer separation propagates upstream in the main flow and forces the shock wave to oscillate, and then the shock oscillation disturbs the boundary layer separation again.

Barakos G, Drikakis D. [2000] investigated a numerical simulation of buffet flows using various turbulence models, including linear and non-linear low-Re eddy-viscosity models (EVM). The study shows that non-linear two-equation models in conjunction with functional Cμ coefficient for the calculation of the eddy-viscosity

(henceforth labelled NL-cμ), provide satisfactory results for transonic buffet flows. The computations also reveal that the Spalart-Allmaras one-equation model provides comparable results to the NL-cμ models, while larger inaccuracies are introduced by linear and non-linear models based on constant Cμ coefficient

Lee B. H. K. [2001] investigated self sustained shock wave motions on airfoil have been experimentally and numerically. Here he described the propagation of the upstream moving waves by solving the non-linear transonic small disturbance equation. He assumed that the flow field can be decomposed into a steady part superimposed with small disturbances. Further he assumed that the upstream moving Kutta waves are small pressure disturbances that are moving at speed of sound with respect to the surrounding flow. With these assumptions it was possible to estimate the travel time of the Kutta waves from the trailing edge to the shock wave position for different flow conditions resulting in an estimation of one part of the buffet cycle. Hereby he refined the idea of self-sustained shock oscillations driven by a closed feed back loop, where one part of the feedback loop is the communication between the trailing edge and the shock via upstream moving pressure waves. A good agreement has been achieved between theoretical and experimental results.

Xiao et al. [2006] investigated buffeting flow over the (BGK No. 1) supercritical airfoil by the solution of the unsteady Reynolds-averaged Navier–Stokes equations with a two-equation lagged k–ω turbulent model. Two steady cases (M= 0.71, α= 1.396 deg and M= 0.71, α= 9.0 deg) and one unsteady case (M= 0.71, α= 6.97 deg), all with a far-stream Reynolds number of 20×10^6, are computed. Self-excited

oscillations of the flow over the BGK No. 1 airfoil are reproduced computationally by this method. The computational results are compared with the experimental data as studied by Lee B. H. K., 2001. Spatial correlations and Fourier transforms of the unsteady disturbances inside and outside the separated boundary layer in the region between the shock wave and airfoil trailing edge are examined to confirm the proposed mechanism by Lee et al.

Deck S. [2005] used a zonal detached eddy simulation (DES) method to predicts the buffet phenomenon on a super- critical airfoil at conditions very near shock buffet onset. Some issues concerning grid generation, as well as the use of DES for thin-layer separation, are discussed. The periodic motion of the shock is well reproduced by averaged Navier Stokes equations (URANS) and zonal DES, but the URANS calculation has needed to increase the angle of attack compared to the experimental value and the standard DES failed to reproduce the self-sustained motion in the present calculation. The main features, including spectral analysis, compare favorably with available experimental measurements.

Bruce P.J.K., Babinsky H. [2008] performed an experimental study of an oscillating shock wave subject to unsteady periodic forcing in a parallel-walled duct. Normal shocks were observed to undergo oscillatory motion in response to an imposed varying pressure ratio. He concluded that the mechanism by which shocks respond to back pressure variations is to change their relative strength by moving so that their relative Mach number matches the pressure jump. These changes in relative shock strength can lead to changes in the extent of boundary layer separation and SBLI

structure. The dynamics of unsteady shock motion measured in experiments were reproduced by a simple inviscid analytical model. A relationship between the amplitude and frequency of shock motion in a diverging duct were outlined, based on the concept of a critical frequency that relates the relative importance of geometry and disturbance frequency on shock dynamics.

Chen et al. [2010] numerically investigated compressible flow past a circular arc aerofoil at free-stream Mach number of 0.76. The detached eddy simulation confirmed the self-sustained shock motions repeated alternately along the upper and lower surfaces of the airfoil, which was identified as type C by Tijdeman and Seebass. Further, due to shock movement on airfoil surface, three typical flow regimes, namely attached boundary layer, moving shock wave/turbulent boundary layer interaction and intermittent boundary layer separation region were recognized during the cycle.

Weber et al. [2002] conducted an experimental and numerical study of the transonic flow through a linear compressor cascade with end walls. The cascade with a low aspect ratio of 1.34 was tested at an inlet Mach number of 1.09 and a Reynolds number of 1.93106. Detailed flow visualizations on the surfaces and five-hole probe measurements inside the balding and in the wake region showed clearly a three-dimensional boundary layer separation on the blade surface and the sidewall, and a severe corner stall induced by a strong 3-D shock system at blade passage entrance.

Weitao et al. [2011] performed a large eddy simulation of complex shock wave boundary layer interaction (SWBLI) in a turbine cascade. The investigation indicated

that, the LES reproduced the SWBLI process accurately. It was found that the SWBLI causes a pressure fluctuation on the suction side downstream of this region and the maximum value was about 2% of the local mean pressure.

Lepicovsky et al. [2004] studied the intermittent flow on the suction surface of an airfoil section from the tip region of a modern low aspect ratio fan blade. Intermittent shock generation makes the flow field bi-stable. As a result, the pressure jumping between two levels impose large intermittent loading on the blade leading edge region and can lead to the onset of blade vibration.

Lepicovsky [2008] performed an extensive experimental study into the nature of the separated flows on the blade suction surface of modern transonic fans. The two observations were made during the study. For subsonic inlet flow, the flow on the suction surface of the blade was separated over a large portion of the blade, and the separated area increased with increasing inlet Mach number. For the supersonic inlet flow condition, the flow was attached from the leading edge up to the point where a bow shock from the upper neighboring blade imposed on the blade surface. Downstream, there was a separated flow region in which air flowed in the direction opposite the inlet flow. Finally, past the separated flow region, the flow reattached to the blade surface.

Becker et al. [2007] performed numerical study to investigate the impact of both the Reynolds number variation and the used turbulence model to capture the boundary layer development on the characteristic of a BR710 fan blade. The investigation

indicated that the interaction between the shock waves of the transonic fan blade row and the boundary layer leads to a significant change of the characteristic.

Hermes et al. [2012] numerically investigated self-induced, unsteady pressure waves propagating over an airfoil transonic flow. The investigation indicated that wake fluctuations are caused by boundary layer vortices from the upper and lower airfoil side interacting with the trailing edge. The generated pressure waves at the trailing edge are high-frequent, three-dimensional and occur stochastically due to the turbulent boundary layer behavior. Wave steepening and nonlinear merging of pressure waves is observed, while the pressure waves are moving upstream against the flow direction.

Xiong et al. [2010] investigated self-excited unsteady transonic flow over a 10% thick circular arc airfoil in a channel using unsteady RANS and DES methods in combination with four different turbulence models. Investigation mentioned that the shock oscillation frequency strongly depends on mean shock wave location.

Raghunathan et al. [2008] reviewed the current understanding of periodic flow by using RANS approach for both a circular arc airfoil and a supercritical airfoil. The effects of boundary layer transition, non adiabatic wall conditions and modifications to the aerofoil surface geometry at the shock interactions on periodic transonic flow are observed. He proposed that the frequency of periodic motion can be predicted with reasonable accuracy, but there are limitations on the prediction of buffet boundaries associated with periodic transonic flows.

Further, the bump control technique were used to reduced wave drag should also reduce buffet for a circular arc airfoil and a supercritical airfoil. In both cases, the bump had a length of 10% and height of 0.2% of aerofoil chord and was located at the mean shock position. It is observed that the fluctuating lift reduces, and correspondingly, the extent of shock motion on the surface. Also reduction in buffet and the chord wise shock motion by 75%. He also proposed that with the bump the frequency of shock motion is increased. The reduced frequency has increased by 50%, from 0.16 to 0.24, the mean shock position has moved from 25% chord to 35% chord closer to the location of the bump and the type of shock motion has changed from the Tijdeman's type B (datum aerofoil) to type A (aerofoil with a bump).

Hasan, A. B. M. Toufique et al. [2009] performed numerical investigation on the effect of non-equilibrium condensation in moist air flow on the characteristics of self-excited shock wave oscillation around a circular arc blade with or without bump on the blade for three different angles of attack. He observed that the shock strength in the case of blade with bump becomes weak compared to that without bump model and the shock induced flow field aerodynamic instabilities such as root mean square (RMS) of pressure oscillation were reduced significantly in case of blade with bump model compared to no bump model.

Flow control is defined by Gad-el-Hak [28] as the ability to actively or passively manipulate a flow field to effect a desired change. The challenge is to achieve that change with a simple device that is inexpensive to build as well as to operate and has minimum side effects. Control of shock wave is possible by both passive and active means. Passive control refers to the ones that require no auxiliary power and no

control loop and sometimes are referred as flow management rather than control. Examples include changing the geometry of the aircraft to increase its aerodynamic properties such as wings equipped with leading edge flaps. These are heavy, require extra hydraulic control and introduce serious problems to sustain the stealth integrity of the aircraft. This type of control is unacceptable in the present case, due to stealth geometry and speed constraints.

On the other hand active flow control refers to the ones where a control loop is used and energy expenditure is required.

The complex phenomena present in the shock-boundary layer interaction region on an aerofoil contribute to increase viscous and shock wave losses, being also, in transonic regime, the main cause of buffet onset. The transonic shock-induced oscillation (SIO) triggered by flow separation behind the shock wave, tends to grow to bounded amplitude, which can reach levels large enough to cause irreversible structural failure. In order to minimize these negative effects induced by buffeting and to decrease the total drag of the aerofoil different control devices have been proposed. There are several control devices proposed to suppressed or delayed shock oscillation on aerofoil and wings at transonic speed [32], and more detail of the flow over an aerofoil with a bump can be found in [29]. These devices are either passive or active and include sub-layer mechanical devices, cavities, bumps, surface cooling devices, vortex generators, boundary layer suction/blowing, continuous or pulse skewed air jets and synthetic jets. Some of the methods of flow control, including adaptive wing technology, have been discussed in detail by several researchers. One of the devices investigated for transonic shock boundary layer interaction is the porous surface with cavity.

Some of the methods of flow control, using adaptive wing technology, have been recently reviewed by Stanewsky and Delery [31].

The aim is to predict numerically buffeting onset, investigating the effect of cavity control technique on aerodynamic characteristics of biconvex aerofoil. The principle of passive control consists in establishing a natural circulation between the downstream high pressure face of a shock and its upstream low pressure face. This circulation is achieved through a cavity, placed underneath the shock foot region.

However, the numerical computations are quite successful tools to predict self sustained shock oscillation over an airfoil in internal transonic flow.

CHAPTER 3

COMPUTATIONAL MODELING AND SIMULATION

3.1 Numerical Method

For investigation of the aerodynamic characteristics, a biconvex circular arc airfoil has been used. The numerical simulation is performed by using Computational Fluid Dynamics (CFD) software. Solving CFD problems usually consists of four main components: geometry and grid generation, setting-up a physical model, solving it and post-processing the computed data.

Two-dimensional Unsteady Navier-Stokes equations were employed for this investigation using a second order upwind implicit predictor/corrector cell-centred finite-volume scheme. A SST k-ω turbulence model is employed. Sutherland's law was used for viscosity and the Prandtl analogy was employed for thermal conductivity. The density based solver with ideal-gas equation was employed for density variations. Second order upwind scheme is used for discretization of flow and turbulence equations (turbulent kinetic energy and specific dissipation rate).

3.2 Computational Study

The equations of fluid dynamics which have been known for over a century are solvable for only a limited number of flows. The known solutions are extremely useful to understand fluid flow. The engineers have traditionally been forced to use other approaches.

In the most common approach, simplifications of the equations are used. These are usually based on a combination of approximations and dimensional

analysis; empirical input is almost always required. In fluid flow analysis, there may require several dimensionless parameters for their specification and it may be impossible to set up an experiment which correctly scales the actual flow.

In other cases, experiments are very difficult if not impossible. For example, the measuring equipment might disturb the flow or the flow may be inaccessible. As technological improvement and competition require more careful optimization of designs or, when new high technology applications demand prediction of flows for which the database is insufficient, experimental development may be too costly and time consuming. Finding a reasonable alternative is essential.

An alternative method came with the birth of electronic computer. Although many of the key ideas for numerical solution methods for partial differential equations were established more than a century ago, they were of little use before computers appeared. Once the power of computers had been recognized, interest in numerical techniques increased dramatically.

3.2.1 Concepts and the Need for CFD

Solution of the equations of fluid dynamics on computers has become so important that it now occupies the attention of perhaps all researchers in fluid mechanics. The field is known as Computational Fluid Dynamics (CFD). The ultimate goal of the field of computational fluid dynamics (CFD) is to understand the physical events that occur in the flow of fluids around and within designated objects. These events are related to the action and interaction of phenomena such as dissipation, diffusion, convection, shock wave, slip surface, boundary layer and turbulence.

CFD provides numerical approximation to the equations that govern fluid motion. Application of the CFD to analyze a fluid problem requires the following steps. First, the mathematical equations describing the fluid flow are written. These are usually a set of partial differential equations. These equations are then discretized to produce a numerical analogue of the equations. The domain is then divided into small grids or elements. Finally, the initial conditions and the boundary conditions of the specific problem are used to solve these equations. The solution method can be direct or iterative. In addition, certain control parameters are used to control the convergence, stability, and accuracy of the method.

Applying the fundamental laws of mechanics to a fluid gives the governing equations for a fluid. The conservation of mass equation and the conservation of momentum equations along with the conservation of energy equation form a set of coupled, nonlinear partial differential equations. It is not possible to solve these equations analytically for most engineering problems. However, it is possible to obtain approximate computer-based solutions to the governing equations for a variety of engineering problems. This is the subject matter of Computational Fluid Dynamics (CFD).

3.2.2 Techniques for Numerical Discretization

In order to solve the governing equations of the fluid motion, at first numerical analogue must be generated. This is done by a process referred to as discretization. In the discretization process, each term within the partial differential equation describing the flow is written in such a manner that the computer can be programmed to calculate. There are various techniques for numerical discretization. Here we will introduce three of the most commonly used techniques, namely:

(1) The finite difference method,

2) The finite element method and

(3) The finite volume method.

Spectral methods are also used in CFD, method of generating a numerical analog of a differential equation is by using fourier series or series of Chebyshev polynomials to approximate the unknown functions. However, most commercial CFD codes use the finite volume or finite-element methods which are better suited for modeling flow past complex geometries. For example, the FLUENT code uses the finite-volume method whereas ANSYS uses the finite-element method.

Broadly, the strategy of CFD is to replace the continuous problem domain with a discrete domain using a grid. In the continuous domain, each flow variable is defined at every point in the domain. For instance, the pressure p in the continuous lD domain shown in the figure below would be given as

$$p = p(x),\ 0 < x < 1$$

In the discrete domain, each flow variable is defined only at the grid points. So, in the discrete domain shown below, the pressure would be defined only at the N grid points.

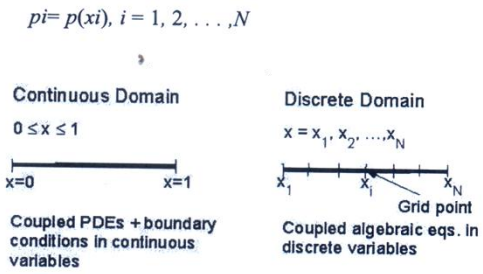

In a CFD solution, one would directly solve for the relevant flow variables only at the grid points. The values at other locations are determined by interpolating the values at the grid points. The governing partial differential equations and boundary conditions are defined in terms of the continuous variables p, V etc. One can approximate these in the discrete domain in terms of the discrete variables P_i, V_i etc. The discrete system is a large set of coupled, algebraic equations in the discrete variables. Setting up the discrete system and solving it (which is a matrix inversion problem) involves a very large number of repetitive calculations and is done by the digital computer. This idea can be extended to any general problem domain.

3.2.3 Discretization Using the Finite-Volume Method

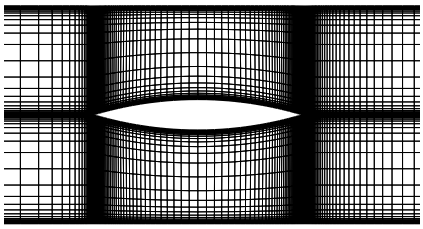

Figure 3.1: Airfoil case grid

The above figure (figure 3.1) shows the grid used for solving the flow over an airfoil. Looking closely at the airfoil grid, it is seen that it consists of quadrilaterals. In the finite-volume method, such a quadrilateral is commonly referred to as a "cell" and a grid point as a "node". In 2D, one could also have triangular cells. In 3D, cells are usually hexahedral, tetrahedral, or prisms. In the finite-volume approach, the integral form of the conservation equations are applied to the control volume defined by a cell to get the discrete equations for the cell. The integral form of the continuity equation for steady, incompressible flow is

$$\int_s \bar{V}.\acute{n}dS = 0 \quad \text{.....(3.1)}$$

The integration is over the surface S of the control volume and n' is the outward normal at the surface. Physically, this equation means that the net volume flow into the control volume is zero. Consider the rectangular cell shown below.

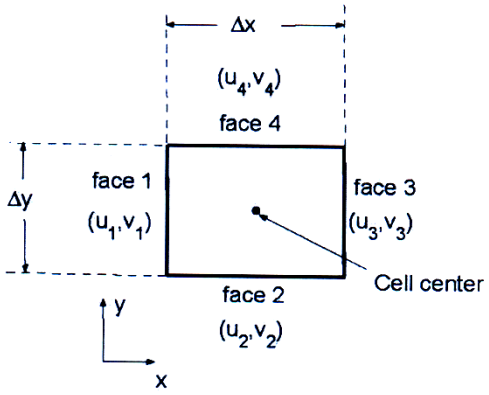

The velocity at face i is taken to be $V_i = u_i i + v_j j$. Applying the mass conservation equation (1) to the control volume defined by the cell gives

$$u_1 \Delta y - v_2 \Delta x + u_3 \Delta y + v_4 \Delta x = 0$$

This is the discrete form of the continuity equation for the cell. It is equivalent to summing up the net mass flow into the control volume and setting it to zero. So it ensures that the net mass flow into the cell is zero i.e. that mass is conserved for the cell. Usually the values at the cell centers are stored. The face values u_1, v_2 etc. are obtained by suitably interpolating the cell-center values at adjacent cells.

Similarly, one can obtain discrete equations for the conservation of momentum and energy for the cell. One can readily extend these ideas to any general cell shape in 2D or 3D and any conservation equation.

3.3 Overview of Flow Solver

CFD allows choosing one of the two numerical methods:

1. Pressure-based solver
2. Density-based solver

The pressure-based approach was developed for low-speed incompressible flows, while the density-based approach was mainly used for high-speed compressible flows. However, recently both methods have been extended and reformulated to solve

and operate for a wide range of flow conditions beyond their traditional or original intent.

In both methods the velocity field is obtained from the momentum equations. In the density based approach, the continuity equation is used to obtain the density field while the pressure field is determined from the equation of state. On the other hand, in the pressure-based approach, the pressure field is extracted by solving a pressure or pressure correction equation which is obtained by manipulating continuity and momentum equations. Using either method, the present CFD tool will solve the governing integral equations for the conservation of mass and momentum, and for energy and other scalars such as turbulence and chemical species. During our numerical analysis we used density based solver. To use the density-based solver, retain the default selection of Density Based Solver.

3.3.1 Ideal Gas Law for Compressible Flows

For compressible flows, the gas law is as following:

$$\rho = \frac{p_{op} + p}{\frac{R}{M}T} \tag{3.2}$$

where,

p = the local relative (or gauge) pressure

p_{op} = the Operating Pressure (set as zero)

3.3.2 Sutherland Viscosity Law

Sutherland's viscosity law resulted from a kinetic theory by Sutherland (1893) using an idealized intermolecular-force potential. The formula is specified using two or three coefficients. Sutherland's law with three coefficients has been used as the form

$$\mu = \mu_0 (\frac{T}{T_0})^{\frac{3}{2}} \frac{T_0 + S}{T + S} \quad (3.3)$$

where,

μ = the viscosity in kg/m-s

T = the static temperature in K

μ_o = reference value in kg/m-s

T_0 = reference temperature in K

S = an effective temperature in K (Sutherland constant)

For air at moderate temperatures and pressures, μ_o= 1.716×10^{-5} kg/m-s, T_0 = 273.11 K, and S = 110.56 K.

3.3.3 Discretization Scheme

The present CFD tool provides Standard, PRESTO, Linear, Second order, Body Force Weighted schemes for Pressure Interpolation Scheme where Second Order was selected for this case. Again for Density, Momentum, Turbulent Kinetic Energy, Specific Dissipation Rate, Energy equations have First Order Upwind, Second Order Upwind, QUICK and Third-Order MUSCL. schemes. For all cases Second Order Upwind schemes were selected.

When the flow is aligned with the grid (e.g., laminar flow in a rectangular duct modeled with a quadrilateral or hexahedral grid) the first-order upwind discretization

is acceptable. When the flow is not aligned with the grid (i.e., when it crosses the grid lines obliquely), however, first order convective discretization increases the numerical discretization error (numerical diffusion). For triangular and tetrahedral grids, since the flow is never aligned with the grid, generally more accurate results are obtained by using the second-order discretization. For quad/hex grids, better results using the second-order discretization is obtained, especially for complex flows.

3.3.4 Pressure-Velocity Coupling

The present CFD tool provides four segregated types of algorithms: SIMPLE, SIMPLEC, PISO, and Fractional Step (FSM). These schemes are referred to as the pressure-based segregated algorithm. Steady-state calculations will generally use SIMPLE or SIMPLEC, while PISO is recommended for transient calculations. In present CFD tool, using the Coupled algorithm enables full pressure-velocity coupling, hence it is referred to as the pressure-based coupled algorithm. This solver offers some advantages over the pressure-based segregated algorithm. The pressure-based coupled algorithm obtains a more robust and efficient single phase implementation for steady-state flows. For choosing Coupled, Courant number had to be specified. For the present numerical study it was set at 0.50.

3.3.5 Explicit and Under-Relaxatioin Factors

The Relaxation Factor field defines the explicit relaxation of variables between sub iterations. The relaxation factors can be used to prevent the solution from diverging. They are left at their default values, unless divergence is detected. If the solution diverges, the solution is stabilized by lowering the relaxation factors.

3.4 Turbulence Modeling:

Whenever turbulence is present in a certain flow it appears to be dominant over all other flow phenomena. That is why successful modeling of turbulence greatly increases the quality of numerical simulations. All analytical and semi-analytical solutions to simple flow cases were already known by the end of 1940s. On the other hand there are still many open questions on modeling turbulence and properties of turbulence it-self. No universal turbulence model exists yet.

Turbulent flows are characterized by fluctuating velocity fields. These fluctuations mix transported quantities such as momentum, energy, and species concentration, and cause the transported quantities to fluctuate as well. Since these fluctuations can be of small scale and high frequency, they are too computationally expensive to simulate directly in practical engineering calculations. Instead, the instantaneous (exact) governing equations can be time-averaged, ensemble-averaged, or otherwise manipulated to remove the small scales, resulting in a modified set of equations that are computationally less expensive to solve. However, the modified equations contain additional unknown variables, and turbulence models are needed to determine these variables in terms of known quantities.

3.4.1 Classes of Turbulence models

Nowadays turbulent flows may be computed using several different approaches. Either by solving the Reynolds-averaged Navier-Stokes equations with suitable models for turbulent quantities or by computing them directly. The main

approaches are summarized below provides the following choices of turbulence models:

1. RANS-based models
    (A) Linear eddy-viscosity models
        (I) Algebraic models
        (II) Spalart-Allmaras (1 equation) model
        (III) Two equation models
            (a) κ-ε models
                (i) Standard *k*-ε model
                (ii) Renormalization-group (RNG) *k*-ε model
                (iii) Realizable *k*-ε model
                (iv) Near-wall Treatment
            (b) *k*-ω models
                (i) Wilcox's k-ω model
                (ii) Wilcox's modified k-ω model
                (iii) Shear-stress transport (SST) k-ω model
    (B) v^2-f model (addon)
    (C) Reynolds stress (5 equations) model (RSM)
            (a) Linear pressure-strain RSM model
            (b) Quadratic pressure-strain RSM model
            (c) Low-Re stress-omega RSM model
2. Detached eddy simulation (DES) model
    (a) Spalart-Allmaras RANS model
    (b) Realizable k-ε RANS model

(c) SST k-ω RANS model

3. Large eddy simulation (LES) model

(a) Smagorinsky-Lilly subgrid-scale model

(b) WALE subgrid-scale model

(c) Kinetic-energy transport subgrid-scale model

4. Direct Numerical Simulation (DNS)

The choice of turbulence model will depend on considerations such as the physics encompassed in the flow, the established practice for a specific class of problem, the level of accuracy required, the available computational resources, and the amount of time available for the simulation.

3.4.2 RANS Equation Averaging

In Reynolds averaging, the solution variables in the instantaneous (exact) Navier- Stokes equations are decomposed into the mean (ensemble-averaged or time-averaged) and fluctuating components. For the velocity components:

$$u_i = \bar{u}_i + \acute{u}_i \tag{3.4}$$

where $\bar{u}_i$ and $\acute{u}_i$ are the mean and fluctuating velocity components (i = 1; 2; 3).

Likewise, for pressure and other scalar quantities:

$$\emptyset = \bar{\emptyset} + \acute{\emptyset} \tag{3.5}$$

where $\emptyset$ denotes a scalar such as pressure, energy, or species concentration. Substituting expressions of this form for the flow variables into the instantaneous continuity and momentum equations and taking a time (or ensemble) average (and dropping the overbear on the mean velocity, $\bar{u}$) yields the ensemble-averaged momentum equations.

They can be written in Cartesian tensor form as:

$$\frac{\delta\rho}{\delta t} + \frac{\delta}{\delta x_i}(\rho u_i) = 0 \tag{3.6}$$

$$\frac{\delta}{\delta t}(\rho u_i) + \frac{\delta}{\delta x_j}(\rho u_i u_j) = -\frac{\delta p}{\delta x_i} + \frac{\delta}{\delta x_j}\left(\mu\left(\frac{\delta u_i}{\delta x_j} + \frac{\delta u_j}{\delta x_i} - \frac{2}{3}\delta_{ij}\frac{\delta u_l}{\delta x_l}\right)\right] + \frac{\delta}{\delta x_j}(-\rho\overline{\acute{u}_i\acute{u}_j})$$

…….. (3.7)

Equations 3.6 and 3.7 are called Reynolds-averaged Navier-Stokes (RANS) equations. They have the same general form as the instantaneous Navier-Stokes equations, with the velocities and other solution variables now representing ensemble-averaged (or time-averaged) values. Additional terms now appear that represent the effects of turbulence. These Reynolds stresses, $-\rho\bar{\acute{u}}_i\bar{\acute{u}}_j$ must be modeled in order to close Equation (3.7)

3.4.3 *k*-ω Model Overview

The k-ω model is one of the most commonly used turbulence models. It is a two equation model that means, it includes two extra transport equations to represent the turbulent properties of the flow. This allows a two equation model to account for history effects like convection and diffusion of turbulent energy.

The first transported variable is turbulent kinetic energy, k. The second transported variable in this case is the specific dissipation, ω. It is the variable that determines the scale of the turbulence, whereas the first variable, k. determines the energy in the turbulence.

3.4.4 Shear-Stress Transport (SST) k-ω Model Overview

The shear-stress transport (SST) k-ω model was developed by Menter [30] to effectively blend the robust and accurate formulation of the k-ω model in the near-wall region with the free-stream independence of the k-ω model in the far field. To achieve this, the k-ε model is converted into a k-ω formulation. The SST k-ω model is similar to the standard k-ω model, but includes the following refinements:

- The standard k-ω model and the transformed k-ε model are both multiplied by a blending function and both models are added together. The blending function is designed to be one in the near-wall region, which activates the standard k-ω model, and zero away from the surface, which activates the transformed k-ε model.
- The SST model incorporates a damped cross-diffusion derivative term in the ω equation.
- The definition of the turbulent viscosity is modified to account for the transport of the turbulent shear stress.
- The modeling constants are different.

These features make the SST k-ω model more accurate and reliable for a wider class of flows (e.g., adverse pressure gradient flows, airfoils, transonic shock waves) than the standard k-ω model. Other modifications include the addition of a cross-diffusion term in the ω equation and a blending function to ensure that the model equations behave appropriately in both the near wall and far field zones.

3.5 Governing Equation for Turbulence Modeling

The flow in this study is considered to be viscous, compressible, turbulent and unsteady. Governing equations for the present numerical simulations are the conservation of mass, conservation of momentum and energy equations written in 2-D coordinate system. Two additional transport equations of k-ω SST (Shear Stress Transport) turbulence model are included to model the turbulence in the flow field. The governing equation can be written in the following vector form:

$$\frac{\delta \boldsymbol{U}}{\delta t} + \frac{\delta \boldsymbol{E}}{\delta x} + \frac{\delta \boldsymbol{F}}{\delta y} = \frac{\delta \boldsymbol{R}}{\delta x} + \frac{\delta \boldsymbol{S}}{\delta y} + \boldsymbol{H} \quad \text{.....(3.8)}$$

Here $\boldsymbol{U}$ is the conservative flux vector. $\boldsymbol{E}$ and $\boldsymbol{F}$ are the inviscid flux vectors and $\boldsymbol{R}$ and $\boldsymbol{S}$ are the viscous flux vectors in the *x* and *y* directions, respectively. $\boldsymbol{H}$ is the source terms corresponding to turbulence. The flux vector and the inviscid flux terms are:

$$\boldsymbol{U}=\begin{bmatrix} \boldsymbol{\rho} \\ \boldsymbol{\rho u} \\ \boldsymbol{E_t} \\ \boldsymbol{\rho k} \\ \boldsymbol{p\omega} \end{bmatrix}, \qquad \boldsymbol{E}=\begin{bmatrix} \boldsymbol{\rho u} \\ \boldsymbol{\rho u^2} \\ \boldsymbol{\rho uv} \\ \boldsymbol{u(E_t + P)} \\ \boldsymbol{\rho uk} \\ \boldsymbol{\rho u\omega} \end{bmatrix} \qquad , \boldsymbol{F}=\begin{bmatrix} \boldsymbol{\rho v} \\ \boldsymbol{\rho uv} \\ \boldsymbol{\rho v^2 + P} \\ \boldsymbol{v(E_t + P)} \\ \boldsymbol{\rho uk} \\ \boldsymbol{pv\omega} \end{bmatrix} \text{.....(3.9)}$$

Here, $\boldsymbol{E_t}$ the total energy, and it can be expressed as:

$$\boldsymbol{E_t = \rho C_P T + \frac{1}{2}\rho(u^2 + v^2)} \text{.....(3.10)}$$

In above equations, $\boldsymbol{\rho}$ is the density, $\boldsymbol{C_p}$ is the specific heat, $\boldsymbol{T}$ is the temperature, *u*- and *v*- are the velocity components in *x*- and *y*- directions, respectively. *k* is turbulence

kinetic energy and ω is specific dissipation rate. *P* is the pressure and it is assumed to follow the ideal gas equation. The viscous terms in Eq. (3.8) are:

$$\boldsymbol{R}=\begin{bmatrix} \boldsymbol{0} \\ \boldsymbol{\tau_{xx}} \\ \boldsymbol{\tau_{xy}} \\ \boldsymbol{\alpha} \\ (\boldsymbol{\mu}+\frac{\boldsymbol{\mu_t}}{\boldsymbol{\sigma_k}})\frac{\boldsymbol{\delta\omega}}{\boldsymbol{\delta x}} \end{bmatrix}, \quad \boldsymbol{S}=\begin{bmatrix} \boldsymbol{0} \\ \boldsymbol{\tau_{xy}} \\ \boldsymbol{\tau_{yy}} \\ \boldsymbol{\beta} \\ \left(\boldsymbol{\mu}+\frac{\boldsymbol{\mu_t}}{\boldsymbol{\sigma_k}}\right)\frac{\boldsymbol{\delta k}}{\boldsymbol{\delta y}} \\ \left(\boldsymbol{\mu}+\frac{\boldsymbol{\mu_t}}{\boldsymbol{\sigma_\omega}}\right)\frac{\boldsymbol{\delta\omega}}{\boldsymbol{\delta y}} \end{bmatrix} \quad \text{.....(3.11)}$$

Where

$$\alpha = u\tau_{xx} + v\tau_{xy} - q_x \quad \text{.....(3.12)}$$

$$\beta = u\tau_{xy} + v\tau_{yy} - q_y \quad \text{.....(3.13)}$$

The stress terms in Eq. (3.10) can now be written as follows:

$$\tau_{xx} = \frac{2}{3}\mu(2\frac{\delta u}{\delta x} - \frac{\delta v}{\delta y} \quad \text{.....(3.14)}$$

$$\tau_{xy} = \mu(\frac{\delta u}{\delta x} + \frac{\delta v}{\delta y}) \quad \text{..... .....(3.15)}$$

$$\tau_{yy} = \frac{2}{3}\mu(2\frac{\delta v}{\delta y} - \frac{\delta u}{\delta x}) \quad \text{.....(3.16)}$$

Under equilibrium conditions, Fourier's law is used to relate the heat transfer rates $\boldsymbol{q_x}$ and $\boldsymbol{q_y}$ with the temperature gradient:

$$q_x = -K\frac{\delta T}{\delta x} \quad \text{.....(3.17)}$$

$$q_y = -K\frac{\delta T}{\delta y} \quad \text{.....(3.18)}$$

The thermal conductivity, *K* can be related to the molecular viscosity, μ using kinetic theory of gases:

$$K = \frac{\mu C_P}{Pr} \quad \text{.....(3.19)}$$

Here *Pr* is the Prandtl number and assumed to be 0.71.

The turbulent viscosity μ_t is calculated as follows:

$$\mu_t = \frac{\rho k}{\omega} \frac{1}{max\left[\frac{1}{\alpha^*}, \frac{SF_2}{\alpha_1 \omega}\right]} \quad \text{.....(3.20)}$$

The coefficient α* damps the turbulent viscosity causing a low-Reynolds-number correction. It is given by

$$\alpha^* = \alpha^*_\infty \left(\frac{\alpha^*_0 + Re_t/R_k}{1 + Re_t/R_k}\right) \quad \text{.....(3.21)}$$

Where, Turbulent Reynolds number, $Re_t = \frac{\rho k}{\mu \omega}$

Model constants $R_{k=6}$, $\alpha^*_0 = \frac{\beta_i}{3}$, $\beta_i = 0.072$, $\alpha_1 = 0.31$

In the high-Reynolds number form of the *k-ω* model, $\alpha^* = \alpha^*_\infty = 1$

Again from eq. (3.19) model constant, $\alpha_1 = 0.31$ and *S* is the modulus of mean rate of strain tensor. The blending function F_2 is given below:

$$F_2 = \tan(\emptyset_2^2) \quad \text{.....(3.22)}$$

$$\emptyset_2 = max\left[2\frac{\sqrt{k}}{0.09\omega y}, \frac{500\mu}{\rho y^2 \omega}\right] \quad \text{.....(3.23)}$$

Where y is the distance to the next surface

The values of turbulent prandtl numbers for k and ω are respectively σ_k and σ_ω which are given by

$$\sigma_k = \frac{1}{\frac{F_1}{\sigma_{k,1}} + (1 - F_1)/\sigma_{k,2}} \quad \text{.....(3.24)}$$

$$\sigma_\omega = \frac{1}{\frac{F_1}{\sigma_{\omega,1}} + (1 - F_1)/\sigma_{\omega,2}} \quad \text{.....(3.25)}$$

Where, model constants are $\sigma_{k,1} = 1.176$, $\sigma_{k,2} = 1.0$ $\sigma_{\omega,1} = 2.0$, $\sigma_{\omega,2} = 1.168$, and the blending function F_1 is given by

$$F_1 = \tan(\emptyset_1^4) \quad \text{.....(3.26)}$$

$$\emptyset_1 = min\left[\max\left(\frac{\sqrt{k}}{0.09\omega y}, \frac{500\mu}{\rho y^2 \omega}\right), \frac{4\rho k}{\sigma_{\omega,2} D^+_\omega y^2}\right] \quad \text{.....(3.27)}$$

D_ω^* is the positive portion of the cross diffusion term D_ω

$$D_\omega = 2(1-F_1)\rho\sigma_{\omega,2}\frac{1}{\omega}\left(\frac{\delta k}{\delta x}+\frac{\delta k}{\delta y}\right)\left(\frac{\delta \omega}{\delta x}+\frac{\delta \omega}{\delta y}\right) \quad \text{.....(3.28)}$$

$$D_\omega^* = \max\left[2\rho\frac{1}{\sigma_{\omega,2}}\frac{1}{\omega}\left(\frac{\delta k}{\delta x}+\frac{\delta k}{\delta y}\right)\left(\frac{\delta \omega}{\delta x}+\frac{\delta \omega}{\delta y}\right), 10^{-10}\right] \quad \text{.....(3.29)}$$

The turbulent source term $\boldsymbol{H}$ in eq. (3.8) is:

$$\boldsymbol{H} = \begin{bmatrix} 0 \\ 0 \\ 0 \\ 0 \\ G_k - Y_k \\ G_\omega - Y_\omega + D_\omega \end{bmatrix} \quad \text{.....(3.30)}$$

In the above equation, G_k is the generation of turbulence kinetic energy due to mean velocity gradients. G_ω represents generation of ω. Y_k is the dissipation of turbulent kinetic energy, k due to turbulence and Y_ω is the dissipation of ω. These functions are determined as follows:

$$G_k = \min(\mu_t S^2, 10\rho\beta^* k\omega) \quad \text{.....(3.31)}$$

Where

$$\beta^* = \beta_i^*[1+\zeta^* F(M_t)] \quad \text{.....(3.32)}$$

$$\beta_i^* = \beta_\infty^*\left[\frac{\frac{4}{15}+\left(\frac{Re_t}{R_\beta}\right)^4}{1+\left(\frac{Re_t}{R_\beta}\right)^4}\right] \quad \text{.....(3.33)}$$

Here, $\zeta^* = 1.5,\ R_\beta = 8,\ \beta_\infty^* = 0.09,\ Re_t = \frac{\rho k}{\mu\omega}$ and

Compressibility function,

$$F(M_t) = \begin{cases} 0, & for\ M_t \le M_{t0} \\ M_t^2 - M_{t0}^2 & for\ M_t > M_{t0} \end{cases} \quad \text{.....(3.34)}$$

Where $M_t^2 = \frac{2k}{a^2},\ a = \sqrt{\gamma RT},\ M_{t0} = 0.25$

Again from eq. (3.30):

$$Y_k = \rho\beta^* k\omega \quad \text{.....(3.35)}$$

$$G_\omega = \frac{\alpha}{v_t} G_k \text{ where } \alpha=1.0 \quad \text{.....(3.36)}$$

$$Y_\omega = \rho\beta\omega^2 \quad \text{.....(3.37)}$$

Where,

$$\beta = \beta_i \left[1 - \frac{\beta_i^*}{\beta_i}\zeta^* F(M_t)\right] \quad \text{.....(3.38)}$$

$$\beta_i = F_1\beta_{i,1} + (1 - F_1)\beta_{i,2} \quad \text{.....(3.39)}$$

$\beta_{i,1} = 0.075$, $\beta_{i,2} = 0.0828$

The governing equations are discretized spatially using a finite volume method of second order scheme. For the time derivatives, an implicit multistage time stepping scheme, which is advanced from time $t + \Delta t$ with a second order Eular backward scheme for physical time and implicit pseudo-time marching scheme for inner iteration, is used. A time step size of 10^{-6} is sufficient for this type of unsteady computation as shown is figure 3.2.

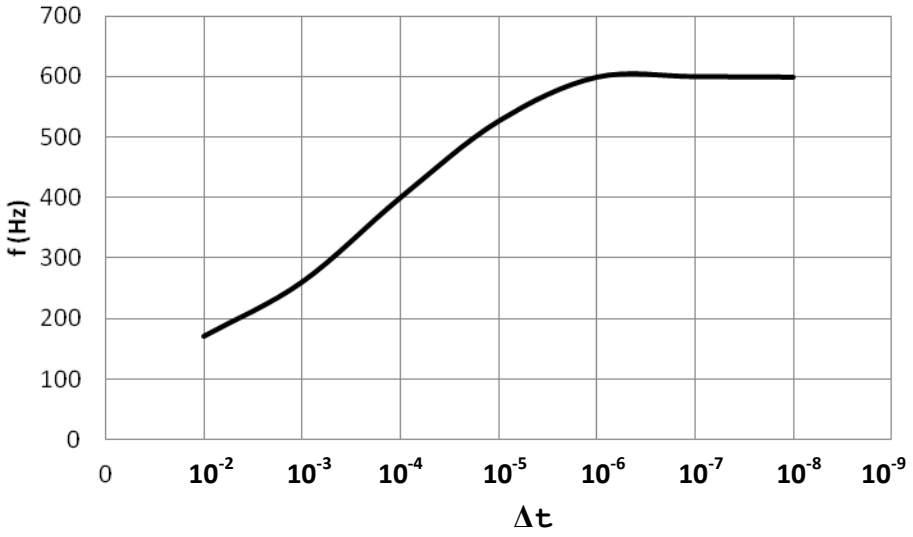

Figure 3.2: Dependency test of time step size for *PR*=0.72

3.6 Descretization of Flow Domain

3.6.1 Create Geometry

The circular arc airfoil geometry was drawn by a preprocessing tool. The airfoil is shown in figure 3.3.

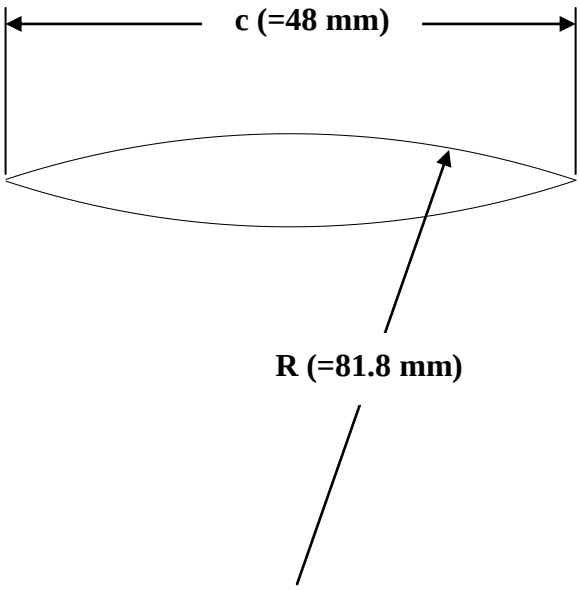

Figure 3.3: Circular Arc airfoil geometry

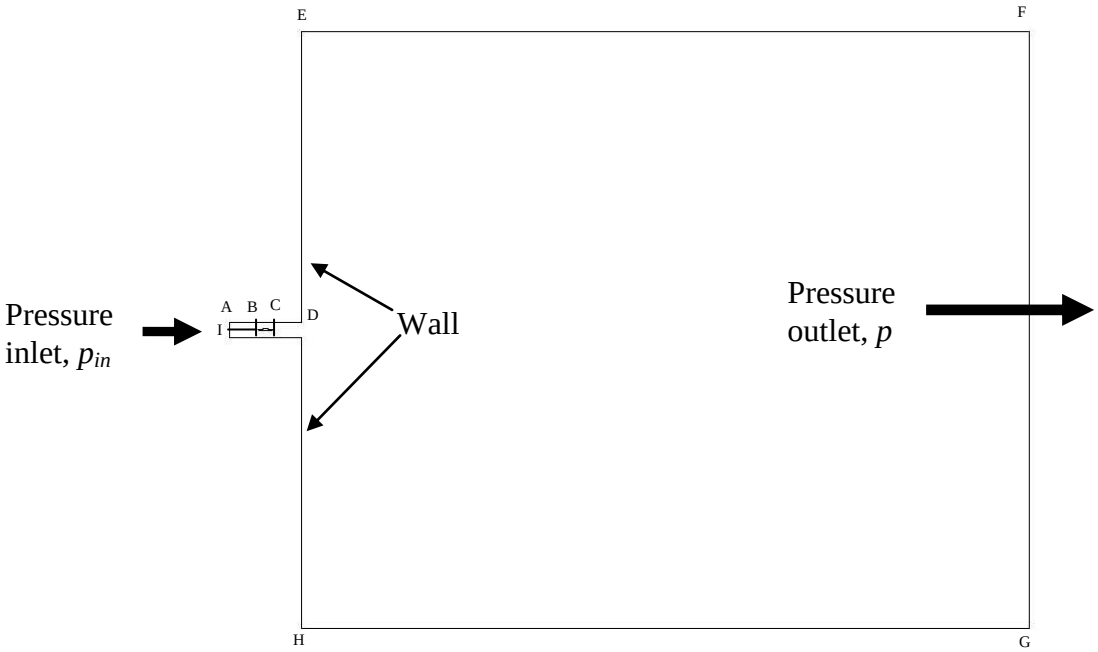

Figure 3.4: Inlet, Outlet and wall boundary around airfoil

Top and bottom wall type boundary was created at 1/2c from the airfoil surfaces. The inlet and outlet boundary was created at 2c and at 52c distance as shown in the figure 3.4. This spacing was considered sufficient to apply free stream conditions on the outer boundaries.

Coordinates of the inlet-outlet boundaries are shown in table 3.1:

Table 3.1: Coordinates of the inlet-outlet boundaries around airfoil.

Label	x-coordinate	y-coordinate
A	-2c	0.5c
B	0	0.5c
C	c	0.5c
D	2c	0.5c
E	2c	20.5c
F	52c	20.5c
G	52c	-20.5c
H	2c	-20.5c
I	-2c	0

3.6.2 Meshing

The matter of grid generation is a significant consideration in CFD. The generation of an appropriate grid of mesh is one thing; the solution of the governing flow equations over such a grid is quite another thing.

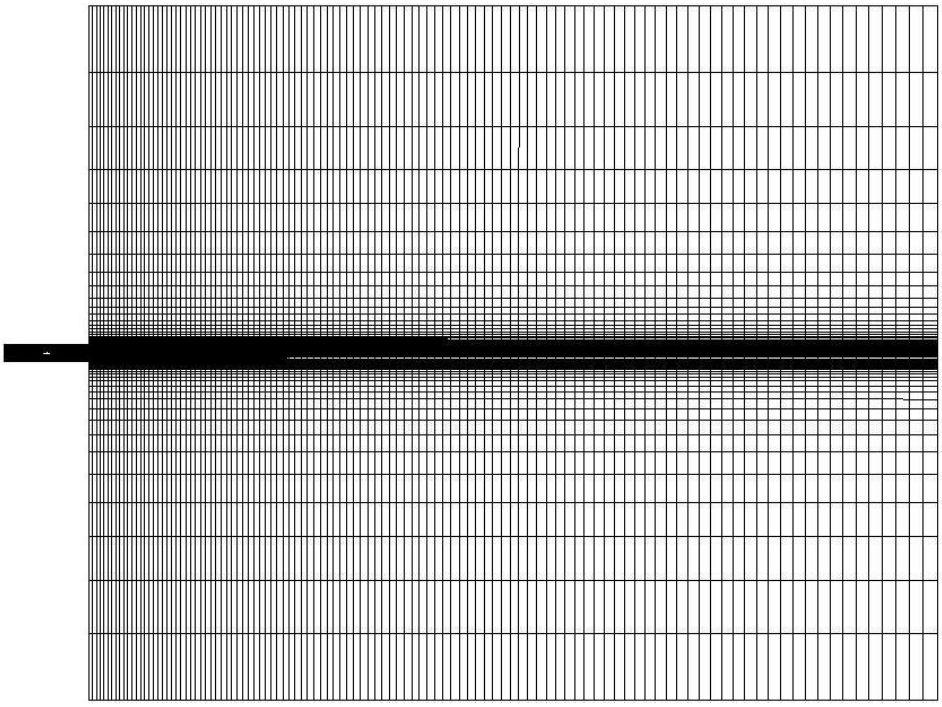

Figure 3.5: Mesh generation around airfoil

As seen from (figure 3.5) that quadrilateral cells were used for this simple geometry because they can be stretched easily to account for different flow gradients in different directions. In the present case, the gradients normal to the airfoil wall are much greater than those tangents to the airfoil. Consequently, the cells near the surface have high aspect ratios. For viscous flow over the airfoil, finely spaced grid was constructed to calculate the details of the flow near the airfoil. The total number

of grid considered is 39800 which give a grid independent solution as shown in figure 3.6.

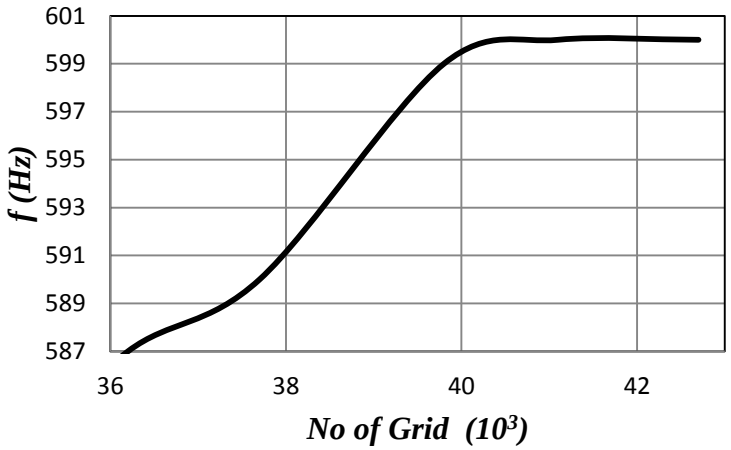

Figure 3.6: Dependency test of No. of Grid for *PR*=0.72.

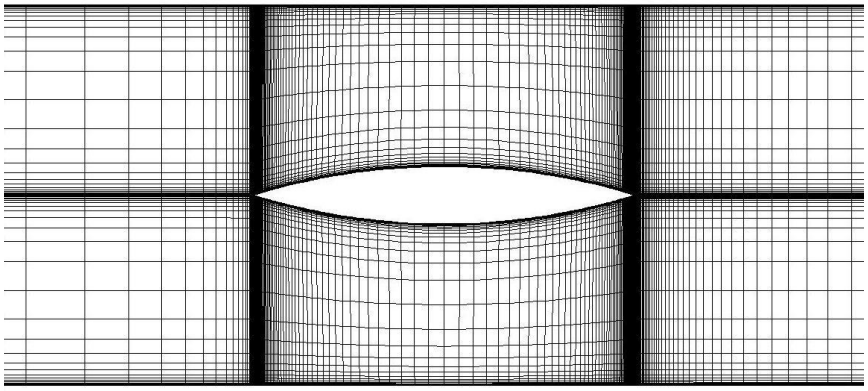

Figure 3.7: Enlarge view of mesh generation around airfoil

Mesh was generated finely around mid chord to capture shock behavior correctly (figure 3.7). As the value of wall y+ in the wall-adjacent cells dictates how wall shear stress is calculated, grid points were selected finely around the airfoil surface to correspond wall y + value less than 1. The values of wall y + are dependent

on the resolution of the grid and the Reynolds number of the flow, and are defined only in wall-adjacent cells.

3.6 Boundary Conditions

Pressure inlet and exit boundary conditions are used to define the fluid pressure at flow inlets respectively, along with all other scalar properties of the flow. They are suitable for both incompressible and compressible flow calculations. Pressure inlet and exit boundary conditions used since the inlet and exit pressure are known but the flow rate and/or velocity is not known. This boundary was used to model a free-stream compressible flow at infinity, with free-stream Mach number and static conditions specified.

In some situations, it is appropriate to specify a uniform value of the turbulence quantity at the boundary where inflow occurs. In most turbulent flows, higher levels of turbulence are generated within shear layers than enter the domain at flow boundaries, making the result of the calculation relatively insensitive to the inflow boundary values. For this reason turbulence specification method was used.

To specify turbulent quantities in terms of the turbulent Intensity and Viscosity Ratio was chosen for k-ω model. The turbulence intensity is defined as the ratio of the root-mean-square of the velocity fluctuations to the mean flow velocity. A turbulence intensity of 1 % or less is generally considered low and turbulence intensities greater than 10% are considered high. Turbulence intensity was selected 5 % and 10%, respectively for inlet and outlet zone. The turbulent viscosity ratio is directly proportional to the turbulent Reynolds number. At the free stream boundaries of most internal flows turbulent viscosity ratio is fairly small. Typically, the turbulence

parameters were set between 1 to 10. Turbulent viscosity ratio was selected 5 and 10, respectively for inlet and outlet zone in the present numerical study.

3.7 Operating Conditions

Operating pressure is significant for low-Mach-number compressible flows because of its role in avoiding round off error problems Operating pressure is less significant for higher-Mach number compressible flows. The pressure changes in such flows are much larger than those in low-Mach-number compressible flows, so there is no real problem with round off error and there is no real need to use gauge pressure. The criteria for choosing a suitable operating pressure are based on the Mach-number regime of the flow and the relationship that is used to determine density. Due transonic regime and density according to ideal gas law operating pressure was set to zero.

3.8 Monitoring Solution Convergence

At the end of each solver iteration, the residual sum for each of the conserved variables is computed and stored, thus recording the convergence history. This history is also saved in the data file. On a computer with infinite precision, these residuals will go to zero as the solution converges. On an actual computer, the residuals decay to some small value and then stop changing. For the present case all residual value was set to 0.00001 for continuity, x velocity, y velocity, energy, turbulent kinetic energy and specific dissipation rate.

3.9 Computational Conditions:

Fig. 3.1-3.7 shows the details of test section. Chord length *c* of the circular arc airfoil is 48 mm. The leading edge and tailing of the airfoil is kept sharp. The thickness t and the radius of the circular arc *R* are 0.15*c* and 1.7*c*, respectively. Computational domain is discretized by structured mesh with (360 x 80) + (110 x 100) = 39800 grid. The minimum normal grid spacing was reduced to 8.34 x 10^{-5} chords, ensuring a value of y^+ <3 everywhere on the airfoil surface. The origin of (x, y) coordinate is located at leading edge of the airfoil. The airfoil is kept at zero angle of attack. The pressure ratio p/p_{in}, where p is total outlet pressure and p_{in} inlet pressure, was varied from 0.71 to 0.75. The inlet Mach numbers upstream of the airfoil are 0.61, 0.61, 0.61, 0.61, and 0.61 for p/p_{in} =0.71, 0.72, 0.73, 0.74, and 0.75 respectively. The following computational conditions were set up for the computational analysis:

At atmospheric conditions, T_∞ =300k, p_{in} =101325 Pa,

For air, ρ=1.176674 kg/m^3, μ= 1.7894×10^{-5} N.s/m^2, v_∞=211.724m/s for M_∞=0.61, c=0.048m. Re=6.68×10^5

CHAPTER 3

COMPUTATIONAL MODELING AND SIMULATION

3.1 Numerical Method

For investigation of the aerodynamic characteristics, a biconvex circular arc airfoil has been used. The numerical simulation is performed by using Computational Fluid Dynamics (CFD) software. Solving CFD problems usually consists of four main components: geometry and grid generation, setting-up a physical model, solving it and post-processing the computed data.

Two-dimensional Unsteady Navier-Stokes equations were employed for this investigation using a second order upwind implicit predictor/corrector cell-centred finite-volume scheme. A SST k-ω turbulence model is employed. Sutherland's law was used for viscosity and the Prandtl analogy was employed for thermal conductivity. The density based solver with ideal-gas equation was employed for density variations. Second order upwind scheme is used for discretization of flow and turbulence equations (turbulent kinetic energy and specific dissipation rate).

3.2 Computational Study

The equations of fluid dynamics which have been known for over a century are solvable for only a limited number of flows. The known solutions are extremely useful to understand fluid flow. The engineers have traditionally been forced to use other approaches.

In the most common approach, simplifications of the equations are used. These are usually based on a combination of approximations and dimensional

analysis; empirical input is almost always required. In fluid flow analysis, there may require several dimensionless parameters for their specification and it may be impossible to set up an experiment which correctly scales the actual flow.

In other cases, experiments are very difficult if not impossible. For example, the measuring equipment might disturb the flow or the flow may be inaccessible. As technological improvement and competition require more careful optimization of designs or, when new high technology applications demand prediction of flows for which the database is insufficient, experimental development may be too costly and time consuming. Finding a reasonable alternative is essential.

An alternative method came with the birth of electronic computer. Although many of the key ideas for numerical solution methods for partial differential equations were established more than a century ago, they were of little use before computers appeared. Once the power of computers had been recognized, interest in numerical techniques increased dramatically.

3.2.1 Concepts and the Need for CFD

Solution of the equations of fluid dynamics on computers has become so important that it now occupies the attention of perhaps all researchers in fluid mechanics. The field is known as Computational Fluid Dynamics (CFD). The ultimate goal of the field of computational fluid dynamics (CFD) is to understand the physical events that occur in the flow of fluids around and within designated objects. These events are related to the action and interaction of phenomena such as dissipation, diffusion, convection, shock wave, slip surface, boundary layer and turbulence.

CFD provides numerical approximation to the equations that govern fluid motion. Application of the CFD to analyze a fluid problem requires the following steps. First, the mathematical equations describing the fluid flow are written. These are usually a set of partial differential equations. These equations are then discretized to produce a numerical analogue of the equations. The domain is then divided into small grids or elements. Finally, the initial conditions and the boundary conditions of the specific problem are used to solve these equations. The solution method can be direct or iterative. In addition, certain control parameters are used to control the convergence, stability, and accuracy of the method.

Applying the fundamental laws of mechanics to a fluid gives the governing equations for a fluid. The conservation of mass equation and the conservation of momentum equations along with the conservation of energy equation form a set of coupled, nonlinear partial differential equations. It is not possible to solve these equations analytically for most engineering problems. However, it is possible to obtain approximate computer-based solutions to the governing equations for a variety of engineering problems. This is the subject matter of Computational Fluid Dynamics (CFD).

3.2.2 Techniques for Numerical Discretization

In order to solve the governing equations of the fluid motion, at first numerical analogue must be generated. This is done by a process referred to as discretization. In the discretization process, each term within the partial differential equation describing the flow is written in such a manner that the computer can be programmed to calculate. There are various techniques for numerical discretization. Here we will introduce three of the most commonly used techniques, namely:

(1) The finite difference method,

2) The finite element method and

(3) The finite volume method.

Spectral methods are also used in CFD, method of generating a numerical analog of a differential equation is by using fourier series or series of Chebyshev polynomials to approximate the unknown functions. However, most commercial CFD codes use the finite volume or finite-element methods which are better suited for modeling flow past complex geometries. For example, the FLUENT code uses the finite-volume method whereas ANSYS uses the finite-element method.

Broadly, the strategy of CFD is to replace the continuous problem domain with a discrete domain using a grid. In the continuous domain, each flow variable is defined at every point in the domain. For instance, the pressure p in the continuous lD domain shown in the figure below would be given as

$$p = p(x),\ 0 < x < 1$$

In the discrete domain, each flow variable is defined only at the grid points. So, in the discrete domain shown below, the pressure would be defined only at the N grid points.

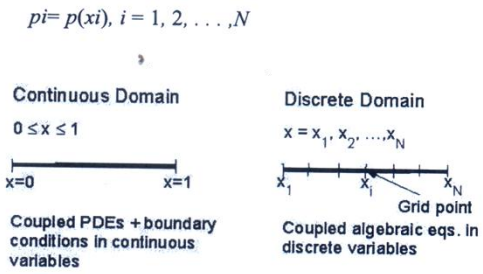

In a CFD solution, one would directly solve for the relevant flow variables only at the grid points. The values at other locations are determined by interpolating the values at the grid points. The governing partial differential equations and boundary conditions are defined in terms of the continuous variables p, V etc. One can approximate these in the discrete domain in terms of the discrete variables P_i, V_i etc. The discrete system is a large set of coupled, algebraic equations in the discrete variables. Setting up the discrete system and solving it (which is a matrix inversion problem) involves a very large number of repetitive calculations and is done by the digital computer. This idea can be extended to any general problem domain.

3.2.3 Discretization Using the Finite-Volume Method

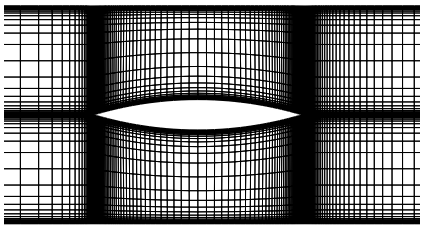

Figure 3.1: Airfoil case grid

The above figure (figure 3.1) shows the grid used for solving the flow over an airfoil. Looking closely at the airfoil grid, it is seen that it consists of quadrilaterals. In the finite-volume method, such a quadrilateral is commonly referred to as a "cell" and a grid point as a "node". In 2D, one could also have triangular cells. In 3D, cells are usually hexahedral, tetrahedral, or prisms. In the finite-volume approach, the integral form of the conservation equations are applied to the control volume defined by a cell to get the discrete equations for the cell. The integral form of the continuity equation for steady, incompressible flow is

$$\int_s \bar{V}.\acute{n}dS = 0 \quad \text{.....(3.1)}$$

The integration is over the surface S of the control volume and n' is the outward normal at the surface. Physically, this equation means that the net volume flow into the control volume is zero. Consider the rectangular cell shown below.

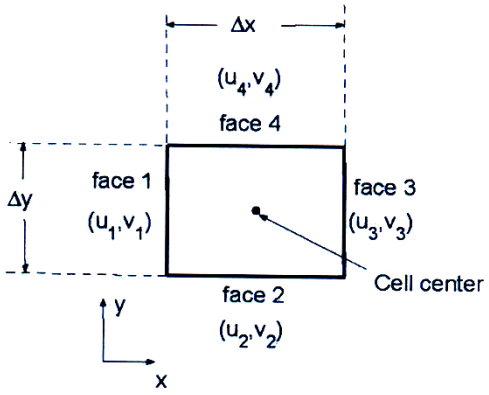

The velocity at face i is taken to be $V_i = u_i i + v_j j$. Applying the mass conservation equation (1) to the control volume defined by the cell gives

$$u_1 \Delta y - v_2 \Delta x + u_3 \Delta y + v_4 \Delta x = 0$$

This is the discrete form of the continuity equation for the cell. It is equivalent to summing up the net mass flow into the control volume and setting it to zero. So it ensures that the net mass flow into the cell is zero i.e. that mass is conserved for the cell. Usually the values at the cell centers are stored. The face values u_1, v_2 etc. are obtained by suitably interpolating the cell-center values at adjacent cells.

Similarly, one can obtain discrete equations for the conservation of momentum and energy for the cell. One can readily extend these ideas to any general cell shape in 2D or 3D and any conservation equation.

3.3 Overview of Flow Solver

CFD allows choosing one of the two numerical methods:

1. Pressure-based solver
2. Density-based solver

The pressure-based approach was developed for low-speed incompressible flows, while the density-based approach was mainly used for high-speed compressible flows. However, recently both methods have been extended and reformulated to solve

and operate for a wide range of flow conditions beyond their traditional or original intent.

In both methods the velocity field is obtained from the momentum equations. In the density based approach, the continuity equation is used to obtain the density field while the pressure field is determined from the equation of state. On the other hand, in the pressure-based approach, the pressure field is extracted by solving a pressure or pressure correction equation which is obtained by manipulating continuity and momentum equations. Using either method, the present CFD tool will solve the governing integral equations for the conservation of mass and momentum, and for energy and other scalars such as turbulence and chemical species. During our numerical analysis we used density based solver. To use the density-based solver, retain the default selection of Density Based Solver.

3.3.1 Ideal Gas Law for Compressible Flows

For compressible flows, the gas law is as following:

$$\rho = \frac{p_{op} + p}{\frac{R}{M}T} \tag{3.2}$$

where,

p = the local relative (or gauge) pressure

p_{op} = the Operating Pressure (set as zero)

3.3.2 Sutherland Viscosity Law

Sutherland's viscosity law resulted from a kinetic theory by Sutherland (1893) using an idealized intermolecular-force potential. The formula is specified using two or three coefficients. Sutherland's law with three coefficients has been used as the form

$$\mu = \mu_0 (\frac{T}{T_0})^{\frac{3}{2}} \frac{T_0 + S}{T + S} \quad (3.3)$$

where,

μ = the viscosity in kg/m-s

T = the static temperature in K

μ_o = reference value in kg/m-s

T_0 = reference temperature in K

S = an effective temperature in K (Sutherland constant)

For air at moderate temperatures and pressures, μ_o= 1.716×10^{-5} kg/m-s, T_0 = 273.11 K, and S = 110.56 K.

3.3.3 Discretization Scheme

The present CFD tool provides Standard, PRESTO, Linear, Second order, Body Force Weighted schemes for Pressure Interpolation Scheme where Second Order was selected for this case. Again for Density, Momentum, Turbulent Kinetic Energy, Specific Dissipation Rate, Energy equations have First Order Upwind, Second Order Upwind, QUICK and Third-Order MUSCL. schemes. For all cases Second Order Upwind schemes were selected.

When the flow is aligned with the grid (e.g., laminar flow in a rectangular duct modeled with a quadrilateral or hexahedral grid) the first-order upwind discretization

is acceptable. When the flow is not aligned with the grid (i.e., when it crosses the grid lines obliquely), however, first order convective discretization increases the numerical discretization error (numerical diffusion). For triangular and tetrahedral grids, since the flow is never aligned with the grid, generally more accurate results are obtained by using the second-order discretization. For quad/hex grids, better results using the second-order discretization is obtained, especially for complex flows.

3.3.4 Pressure-Velocity Coupling

The present CFD tool provides four segregated types of algorithms: SIMPLE, SIMPLEC, PISO, and Fractional Step (FSM). These schemes are referred to as the pressure-based segregated algorithm. Steady-state calculations will generally use SIMPLE or SIMPLEC, while PISO is recommended for transient calculations. In present CFD tool, using the Coupled algorithm enables full pressure-velocity coupling, hence it is referred to as the pressure-based coupled algorithm. This solver offers some advantages over the pressure-based segregated algorithm. The pressure-based coupled algorithm obtains a more robust and efficient single phase implementation for steady-state flows. For choosing Coupled, Courant number had to be specified. For the present numerical study it was set at 0.50.

3.3.5 Explicit and Under-Relaxatioin Factors

The Relaxation Factor field defines the explicit relaxation of variables between sub iterations. The relaxation factors can be used to prevent the solution from diverging. They are left at their default values, unless divergence is detected. If the solution diverges, the solution is stabilized by lowering the relaxation factors.

3.4 Turbulence Modeling:

Whenever turbulence is present in a certain flow it appears to be dominant over all other flow phenomena. That is why successful modeling of turbulence greatly increases the quality of numerical simulations. All analytical and semi-analytical solutions to simple flow cases were already known by the end of 1940s. On the other hand there are still many open questions on modeling turbulence and properties of turbulence it-self. No universal turbulence model exists yet.

Turbulent flows are characterized by fluctuating velocity fields. These fluctuations mix transported quantities such as momentum, energy, and species concentration, and cause the transported quantities to fluctuate as well. Since these fluctuations can be of small scale and high frequency, they are too computationally expensive to simulate directly in practical engineering calculations. Instead, the instantaneous (exact) governing equations can be time-averaged, ensemble-averaged, or otherwise manipulated to remove the small scales, resulting in a modified set of equations that are computationally less expensive to solve. However, the modified equations contain additional unknown variables, and turbulence models are needed to determine these variables in terms of known quantities.

3.4.1 Classes of Turbulence models

Nowadays turbulent flows may be computed using several different approaches. Either by solving the Reynolds-averaged Navier-Stokes equations with suitable models for turbulent quantities or by computing them directly. The main

approaches are summarized below provides the following choices of turbulence models:

1. RANS-based models
    (A) Linear eddy-viscosity models
        (I) Algebraic models
        (II) Spalart-Allmaras (1 equation) model
        (III) Two equation models
            (a) κ-ε models
                (i) Standard *k*-ε model
                (ii) Renormalization-group (RNG) *k*-ε model
                (iii) Realizable *k*-ε model
                (iv) Near-wall Treatment
            (b) *k*-ω models
                (i) Wilcox's k-ω model
                (ii) Wilcox's modified k-ω model
                (iii) Shear-stress transport (SST) k-ω model
    (B) v^2-f model (addon)
    (C) Reynolds stress (5 equations) model (RSM)
            (a) Linear pressure-strain RSM model
            (b) Quadratic pressure-strain RSM model
            (c) Low-Re stress-omega RSM model
2. Detached eddy simulation (DES) model
    (a) Spalart-Allmaras RANS model
    (b) Realizable k-ε RANS model

(c) SST k-ω RANS model

3. Large eddy simulation (LES) model

(a) Smagorinsky-Lilly subgrid-scale model

(b) WALE subgrid-scale model

(c) Kinetic-energy transport subgrid-scale model

4. Direct Numerical Simulation (DNS)

The choice of turbulence model will depend on considerations such as the physics encompassed in the flow, the established practice for a specific class of problem, the level of accuracy required, the available computational resources, and the amount of time available for the simulation.

3.4.2 RANS Equation Averaging

In Reynolds averaging, the solution variables in the instantaneous (exact) Navier- Stokes equations are decomposed into the mean (ensemble-averaged or time-averaged) and fluctuating components. For the velocity components:

$$u_i = \bar{u}_i + \acute{u}_i \tag{3.4}$$

where $\bar{u}_i$ and $\acute{u}_i$ are the mean and fluctuating velocity components (i = 1; 2; 3).

Likewise, for pressure and other scalar quantities:

$$\emptyset = \bar{\emptyset} + \acute{\emptyset} \tag{3.5}$$

where $\emptyset$ denotes a scalar such as pressure, energy, or species concentration. Substituting expressions of this form for the flow variables into the instantaneous continuity and momentum equations and taking a time (or ensemble) average (and dropping the overbear on the mean velocity, $\bar{u}$) yields the ensemble-averaged momentum equations.

They can be written in Cartesian tensor form as:

$$\frac{\delta\rho}{\delta t} + \frac{\delta}{\delta x_i}(\rho u_i) = 0 \tag{3.6}$$

$$\frac{\delta}{\delta t}(\rho u_i) + \frac{\delta}{\delta x_j}(\rho u_i u_j) = -\frac{\delta p}{\delta x_i} + \frac{\delta}{\delta x_j}\left(\mu\left(\frac{\delta u_i}{\delta x_j} + \frac{\delta u_j}{\delta x_i} - \frac{2}{3}\delta_{ij}\frac{\delta u_l}{\delta x_l}\right)\right] + \frac{\delta}{\delta x_j}(-\rho\overline{\acute{u}_i\acute{u}_j})$$

…….. (3.7)

Equations 3.6 and 3.7 are called Reynolds-averaged Navier-Stokes (RANS) equations. They have the same general form as the instantaneous Navier-Stokes equations, with the velocities and other solution variables now representing ensemble-averaged (or time-averaged) values. Additional terms now appear that represent the effects of turbulence. These Reynolds stresses, $-\rho\bar{\acute{u}}_i\bar{\acute{u}}_j$ must be modeled in order to close Equation (3.7)

3.4.3 *k*-ω Model Overview

The k-ω model is one of the most commonly used turbulence models. It is a two equation model that means, it includes two extra transport equations to represent the turbulent properties of the flow. This allows a two equation model to account for history effects like convection and diffusion of turbulent energy.

The first transported variable is turbulent kinetic energy, k. The second transported variable in this case is the specific dissipation, ω. It is the variable that determines the scale of the turbulence, whereas the first variable, k. determines the energy in the turbulence.

3.4.4 Shear-Stress Transport (SST) k-ω Model Overview

The shear-stress transport (SST) k-ω model was developed by Menter [30] to effectively blend the robust and accurate formulation of the k-ω model in the near-wall region with the free-stream independence of the k-ω model in the far field. To achieve this, the k-ε model is converted into a k-ω formulation. The SST k-ω model is similar to the standard k-ω model, but includes the following refinements:

- The standard k-ω model and the transformed k-ε model are both multiplied by a blending function and both models are added together. The blending function is designed to be one in the near-wall region, which activates the standard k-ω model, and zero away from the surface, which activates the transformed k-ε model.
- The SST model incorporates a damped cross-diffusion derivative term in the ω equation.
- The definition of the turbulent viscosity is modified to account for the transport of the turbulent shear stress.
- The modeling constants are different.

These features make the SST k-ω model more accurate and reliable for a wider class of flows (e.g., adverse pressure gradient flows, airfoils, transonic shock waves) than the standard k-ω model. Other modifications include the addition of a cross-diffusion term in the ω equation and a blending function to ensure that the model equations behave appropriately in both the near wall and far field zones.

3.5 Governing Equation for Turbulence Modeling

The flow in this study is considered to be viscous, compressible, turbulent and unsteady. Governing equations for the present numerical simulations are the conservation of mass, conservation of momentum and energy equations written in 2-D coordinate system. Two additional transport equations of k-ω SST (Shear Stress Transport) turbulence model are included to model the turbulence in the flow field. The governing equation can be written in the following vector form:

$$\frac{\delta \boldsymbol{U}}{\delta t} + \frac{\delta \boldsymbol{E}}{\delta x} + \frac{\delta \boldsymbol{F}}{\delta y} = \frac{\delta \boldsymbol{R}}{\delta x} + \frac{\delta \boldsymbol{S}}{\delta y} + \boldsymbol{H} \quad \text{.....(3.8)}$$

Here $\boldsymbol{U}$ is the conservative flux vector. $\boldsymbol{E}$ and $\boldsymbol{F}$ are the inviscid flux vectors and $\boldsymbol{R}$ and $\boldsymbol{S}$ are the viscous flux vectors in the *x* and *y* directions, respectively. $\boldsymbol{H}$ is the source terms corresponding to turbulence. The flux vector and the inviscid flux terms are:

$$\boldsymbol{U}=\begin{bmatrix} \boldsymbol{\rho} \\ \boldsymbol{\rho u} \\ \boldsymbol{E_t} \\ \boldsymbol{\rho k} \\ \boldsymbol{p\omega} \end{bmatrix}, \qquad \boldsymbol{E}=\begin{bmatrix} \boldsymbol{\rho u} \\ \boldsymbol{\rho u^2} \\ \boldsymbol{\rho uv} \\ \boldsymbol{u(E_t + P)} \\ \boldsymbol{\rho uk} \\ \boldsymbol{\rho u\omega} \end{bmatrix} \qquad , \boldsymbol{F}=\begin{bmatrix} \boldsymbol{\rho v} \\ \boldsymbol{\rho uv} \\ \boldsymbol{\rho v^2 + P} \\ \boldsymbol{v(E_t + P)} \\ \boldsymbol{\rho uk} \\ \boldsymbol{pv\omega} \end{bmatrix} \text{.....(3.9)}$$

Here, $\boldsymbol{E_t}$ the total energy, and it can be expressed as:

$$\boldsymbol{E_t = \rho C_P T + \frac{1}{2}\rho(u^2 + v^2)} \text{.....(3.10)}$$

In above equations, $\boldsymbol{\rho}$ is the density, $\boldsymbol{C_p}$ is the specific heat, $\boldsymbol{T}$ is the temperature, *u*- and *v*- are the velocity components in *x*- and *y*- directions, respectively. *k* is turbulence

kinetic energy and ω is specific dissipation rate. *P* is the pressure and it is assumed to follow the ideal gas equation. The viscous terms in Eq. (3.8) are:

$$\boldsymbol{R}=\begin{bmatrix} \boldsymbol{0} \\ \boldsymbol{\tau_{xx}} \\ \boldsymbol{\tau_{xy}} \\ \boldsymbol{\alpha} \\ (\boldsymbol{\mu}+\frac{\boldsymbol{\mu_t}}{\boldsymbol{\sigma_k}})\frac{\boldsymbol{\delta\omega}}{\boldsymbol{\delta x}} \end{bmatrix}, \quad \boldsymbol{S}=\begin{bmatrix} \boldsymbol{0} \\ \boldsymbol{\tau_{xy}} \\ \boldsymbol{\tau_{yy}} \\ \boldsymbol{\beta} \\ \left(\boldsymbol{\mu}+\frac{\boldsymbol{\mu_t}}{\boldsymbol{\sigma_k}}\right)\frac{\boldsymbol{\delta k}}{\boldsymbol{\delta y}} \\ \left(\boldsymbol{\mu}+\frac{\boldsymbol{\mu_t}}{\boldsymbol{\sigma_\omega}}\right)\frac{\boldsymbol{\delta\omega}}{\boldsymbol{\delta y}} \end{bmatrix} \quad \text{.....(3.11)}$$

Where

$$\alpha = u\tau_{xx} + v\tau_{xy} - q_x \quad \text{.....(3.12)}$$

$$\beta = u\tau_{xy} + v\tau_{yy} - q_y \quad \text{.....(3.13)}$$

The stress terms in Eq. (3.10) can now be written as follows:

$$\tau_{xx} = \frac{2}{3}\mu(2\frac{\delta u}{\delta x} - \frac{\delta v}{\delta y} \quad \text{.....(3.14)}$$

$$\tau_{xy} = \mu(\frac{\delta u}{\delta x} + \frac{\delta v}{\delta y}) \quad \text{..... .....(3.15)}$$

$$\tau_{yy} = \frac{2}{3}\mu(2\frac{\delta v}{\delta y} - \frac{\delta u}{\delta x}) \quad \text{.....(3.16)}$$

Under equilibrium conditions, Fourier's law is used to relate the heat transfer rates $\boldsymbol{q_x}$ and $\boldsymbol{q_y}$ with the temperature gradient:

$$q_x = -K\frac{\delta T}{\delta x} \quad \text{.....(3.17)}$$

$$q_y = -K\frac{\delta T}{\delta y} \quad \text{.....(3.18)}$$

The thermal conductivity, *K* can be related to the molecular viscosity, μ using kinetic theory of gases:

$$K = \frac{\mu C_P}{Pr} \quad \text{.....(3.19)}$$

Here *Pr* is the Prandtl number and assumed to be 0.71.

The turbulent viscosity μ_t is calculated as follows:

$$\mu_t = \frac{\rho k}{\omega} \frac{1}{max\left[\frac{1}{\alpha^*}, \frac{SF_2}{\alpha_1 \omega}\right]} \quad \text{.....(3.20)}$$

The coefficient α* damps the turbulent viscosity causing a low-Reynolds-number correction. It is given by

$$\alpha^* = \alpha^*_\infty \left(\frac{\alpha^*_0 + Re_t/R_k}{1 + Re_t/R_k}\right) \quad \text{.....(3.21)}$$

Where, Turbulent Reynolds number, $Re_t = \frac{\rho k}{\mu \omega}$

Model constants $R_{k=6}$, $\alpha^*_0 = \frac{\beta_i}{3}$, $\beta_i = 0.072$, $\alpha_1 = 0.31$

In the high-Reynolds number form of the *k-ω* model, $\alpha^* = \alpha^*_\infty = 1$

Again from eq. (3.19) model constant, $\alpha_1 = 0.31$ and *S* is the modulus of mean rate of strain tensor. The blending function F_2 is given below:

$$F_2 = \tan(\emptyset_2^2) \quad \text{.....(3.22)}$$

$$\emptyset_2 = max\left[2\frac{\sqrt{k}}{0.09\omega y}, \frac{500\mu}{\rho y^2 \omega}\right] \quad \text{.....(3.23)}$$

Where y is the distance to the next surface

The values of turbulent prandtl numbers for k and ω are respectively σ_k and σ_ω which are given by

$$\sigma_k = \frac{1}{\frac{F_1}{\sigma_{k,1}} + (1 - F_1)/\sigma_{k,2}} \quad \text{.....(3.24)}$$

$$\sigma_\omega = \frac{1}{\frac{F_1}{\sigma_{\omega,1}} + (1 - F_1)/\sigma_{\omega,2}} \quad \text{.....(3.25)}$$

Where, model constants are $\sigma_{k,1} = 1.176$, $\sigma_{k,2} = 1.0$ $\sigma_{\omega,1} = 2.0$, $\sigma_{\omega,2} = 1.168$, and the blending function F_1 is given by

$$F_1 = \tan(\emptyset_1^4) \quad \text{.....(3.26)}$$

$$\emptyset_1 = min\left[\max\left(\frac{\sqrt{k}}{0.09\omega y}, \frac{500\mu}{\rho y^2 \omega}\right), \frac{4\rho k}{\sigma_{\omega,2} D^+_\omega y^2}\right] \quad \text{.....(3.27)}$$

D_ω^* is the positive portion of the cross diffusion term D_ω

$$D_\omega = 2(1-F_1)\rho\sigma_{\omega,2}\frac{1}{\omega}\left(\frac{\delta k}{\delta x}+\frac{\delta k}{\delta y}\right)\left(\frac{\delta \omega}{\delta x}+\frac{\delta \omega}{\delta y}\right) \quad \text{.....(3.28)}$$

$$D_\omega^* = \max\left[2\rho\frac{1}{\sigma_{\omega,2}}\frac{1}{\omega}\left(\frac{\delta k}{\delta x}+\frac{\delta k}{\delta y}\right)\left(\frac{\delta \omega}{\delta x}+\frac{\delta \omega}{\delta y}\right), 10^{-10}\right] \quad \text{.....(3.29)}$$

The turbulent source term $\boldsymbol{H}$ in eq. (3.8) is:

$$\boldsymbol{H} = \begin{bmatrix} 0 \\ 0 \\ 0 \\ 0 \\ G_k - Y_k \\ G_\omega - Y_\omega + D_\omega \end{bmatrix} \quad \text{.....(3.30)}$$

In the above equation, G_k is the generation of turbulence kinetic energy due to mean velocity gradients. G_ω represents generation of ω. Y_k is the dissipation of turbulent kinetic energy, k due to turbulence and Y_ω is the dissipation of ω. These functions are determined as follows:

$$G_k = \min(\mu_t S^2, 10\rho\beta^* k\omega) \quad \text{.....(3.31)}$$

Where

$$\beta^* = \beta_i^*[1+\zeta^* F(M_t)] \quad \text{.....(3.32)}$$

$$\beta_i^* = \beta_\infty^*\left[\frac{\frac{4}{15}+\left(\frac{Re_t}{R_\beta}\right)^4}{1+\left(\frac{Re_t}{R_\beta}\right)^4}\right] \quad \text{.....(3.33)}$$

Here, $\zeta^* = 1.5,\ R_\beta = 8,\ \beta_\infty^* = 0.09,\ Re_t = \frac{\rho k}{\mu\omega}$ and

Compressibility function,

$$F(M_t) = \begin{cases} 0, & for\ M_t \le M_{t0} \\ M_t^2 - M_{t0}^2 & for\ M_t > M_{t0} \end{cases} \quad \text{.....(3.34)}$$

Where $M_t^2 = \frac{2k}{a^2},\ a = \sqrt{\gamma RT},\ M_{t0} = 0.25$

Again from eq. (3.30):

$$Y_k = \rho\beta^* k\omega \quad \text{.....(3.35)}$$

$$G_\omega = \frac{\alpha}{v_t} G_k \text{ where } \alpha=1.0 \quad \text{.....(3.36)}$$

$$Y_\omega = \rho\beta\omega^2 \quad \text{.....(3.37)}$$

Where,

$$\beta = \beta_i \left[1 - \frac{\beta_i^*}{\beta_i}\zeta^* F(M_t)\right] \quad \text{.....(3.38)}$$

$$\beta_i = F_1\beta_{i,1} + (1 - F_1)\beta_{i,2} \quad \text{.....(3.39)}$$

$\beta_{i,1} = 0.075$, $\beta_{i,2} = 0.0828$

The governing equations are discretized spatially using a finite volume method of second order scheme. For the time derivatives, an implicit multistage time stepping scheme, which is advanced from time $t + \Delta t$ with a second order Eular backward scheme for physical time and implicit pseudo-time marching scheme for inner iteration, is used. A time step size of 10^{-6} is sufficient for this type of unsteady computation as shown is figure 3.2.

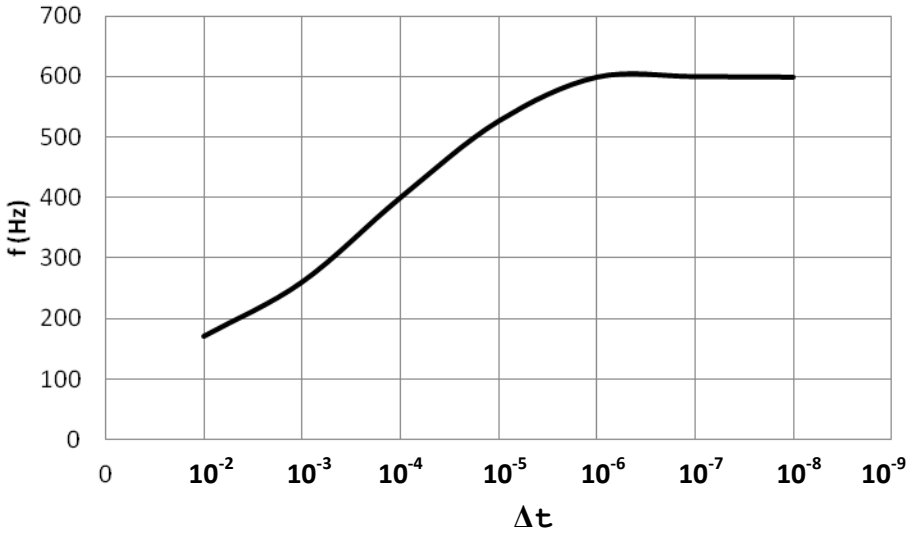

Figure 3.2: Dependency test of time step size for *PR*=0.72

3.6 Descretization of Flow Domain

3.6.1 Create Geometry

The circular arc airfoil geometry was drawn by a preprocessing tool. The airfoil is shown in figure 3.3.

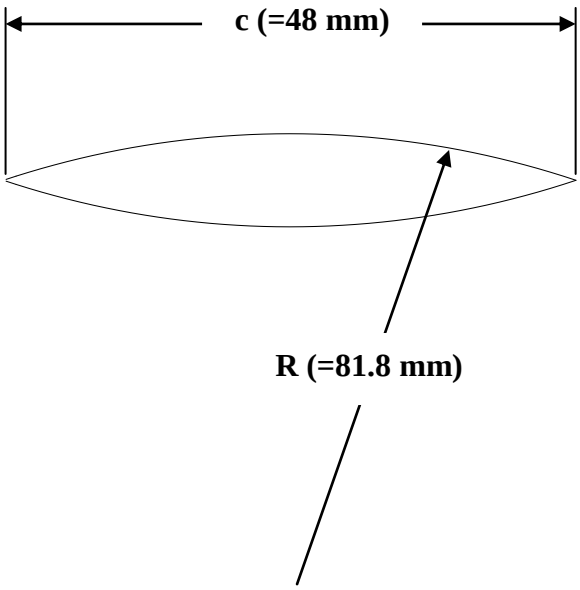

Figure 3.3: Circular Arc airfoil geometry

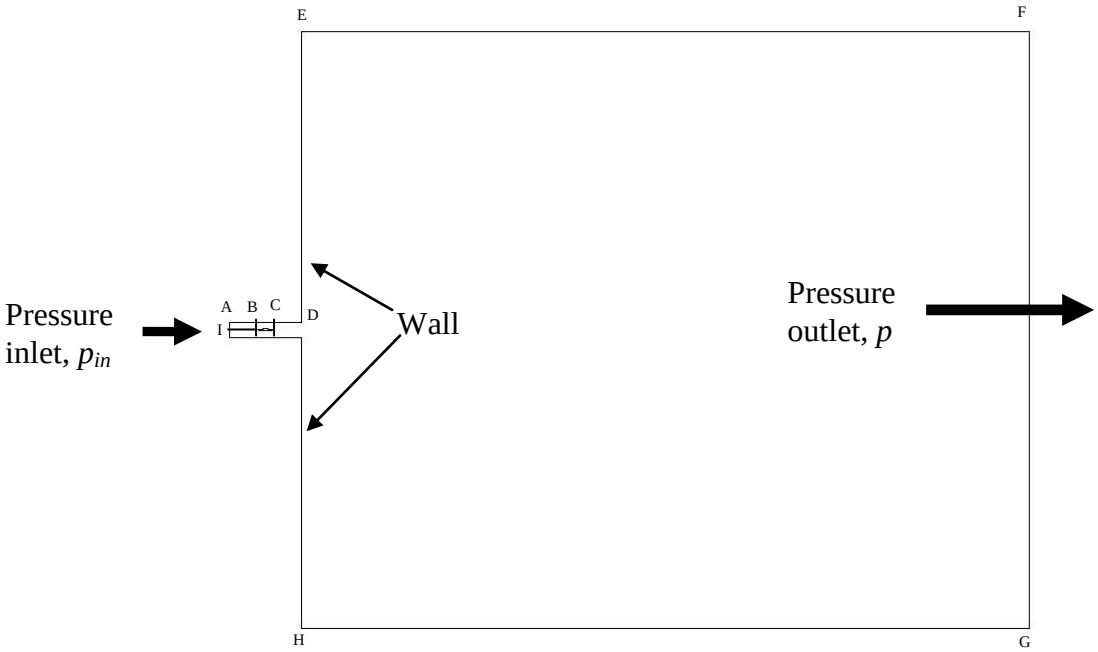

Figure 3.4: Inlet, Outlet and wall boundary around airfoil

Top and bottom wall type boundary was created at 1/2c from the airfoil surfaces. The inlet and outlet boundary was created at 2c and at 52c distance as shown in the figure 3.4. This spacing was considered sufficient to apply free stream conditions on the outer boundaries.

Coordinates of the inlet-outlet boundaries are shown in table 3.1:

Table 3.1: Coordinates of the inlet-outlet boundaries around airfoil.

Label	x-coordinate	y-coordinate
A	-2c	0.5c
B	0	0.5c
C	c	0.5c
D	2c	0.5c
E	2c	20.5c
F	52c	20.5c
G	52c	-20.5c
H	2c	-20.5c
I	-2c	0

3.6.2 Meshing

The matter of grid generation is a significant consideration in CFD. The generation of an appropriate grid of mesh is one thing; the solution of the governing flow equations over such a grid is quite another thing.

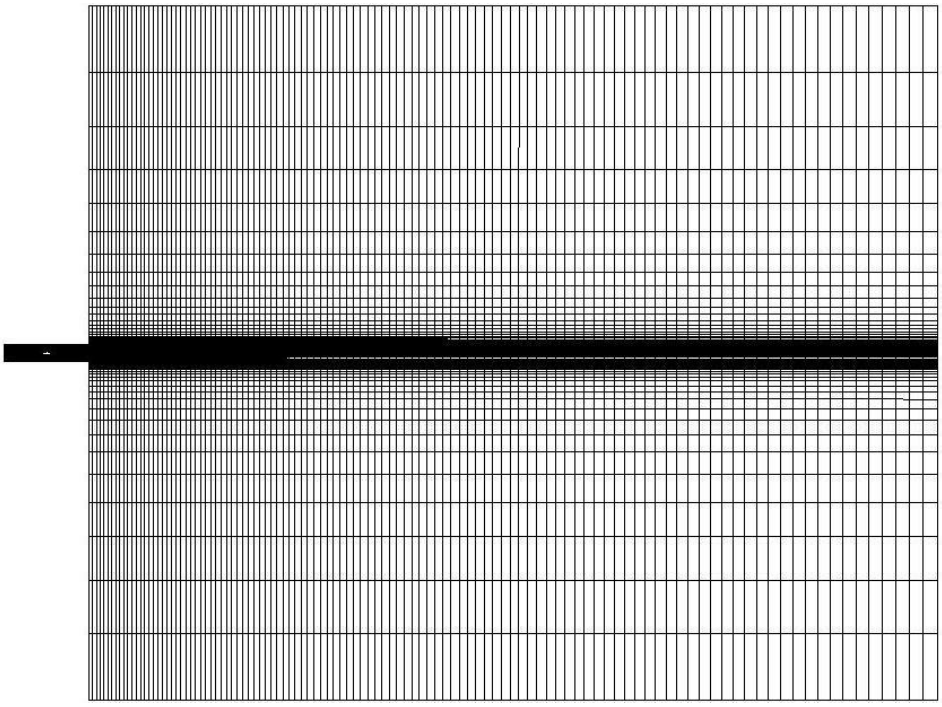

Figure 3.5: Mesh generation around airfoil

As seen from (figure 3.5) that quadrilateral cells were used for this simple geometry because they can be stretched easily to account for different flow gradients in different directions. In the present case, the gradients normal to the airfoil wall are much greater than those tangents to the airfoil. Consequently, the cells near the surface have high aspect ratios. For viscous flow over the airfoil, finely spaced grid was constructed to calculate the details of the flow near the airfoil. The total number

of grid considered is 39800 which give a grid independent solution as shown in figure 3.6.

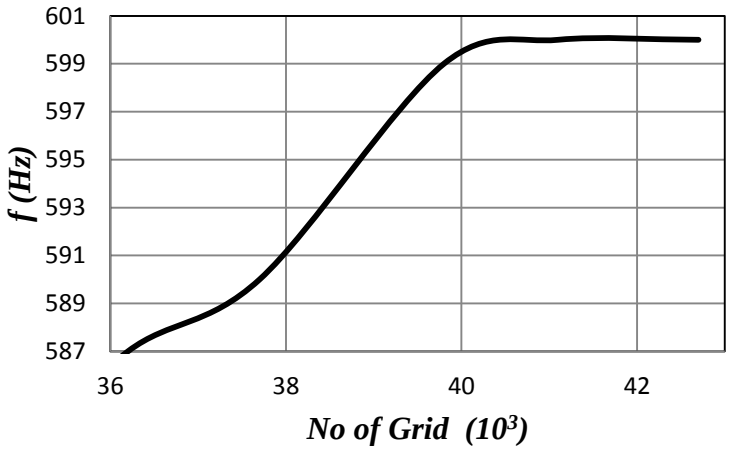

Figure 3.6: Dependency test of No. of Grid for *PR*=0.72.

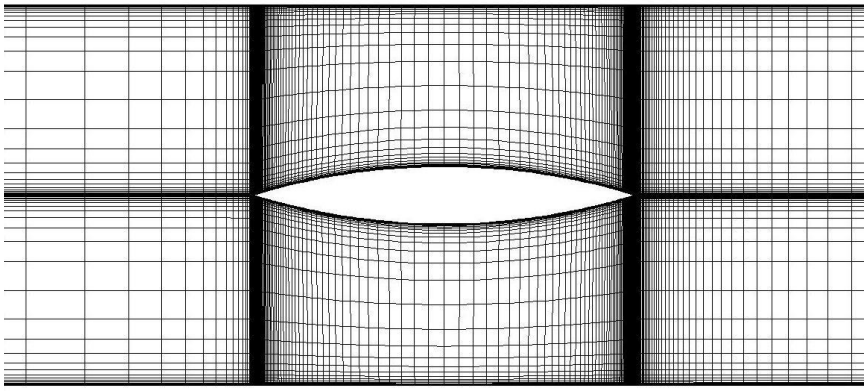

Figure 3.7: Enlarge view of mesh generation around airfoil

Mesh was generated finely around mid chord to capture shock behavior correctly (figure 3.7). As the value of wall y+ in the wall-adjacent cells dictates how wall shear stress is calculated, grid points were selected finely around the airfoil surface to correspond wall y + value less than 1. The values of wall y + are dependent

on the resolution of the grid and the Reynolds number of the flow, and are defined only in wall-adjacent cells.

3.6 Boundary Conditions

Pressure inlet and exit boundary conditions are used to define the fluid pressure at flow inlets respectively, along with all other scalar properties of the flow. They are suitable for both incompressible and compressible flow calculations. Pressure inlet and exit boundary conditions used since the inlet and exit pressure are known but the flow rate and/or velocity is not known. This boundary was used to model a free-stream compressible flow at infinity, with free-stream Mach number and static conditions specified.

In some situations, it is appropriate to specify a uniform value of the turbulence quantity at the boundary where inflow occurs. In most turbulent flows, higher levels of turbulence are generated within shear layers than enter the domain at flow boundaries, making the result of the calculation relatively insensitive to the inflow boundary values. For this reason turbulence specification method was used.

To specify turbulent quantities in terms of the turbulent Intensity and Viscosity Ratio was chosen for k-ω model. The turbulence intensity is defined as the ratio of the root-mean-square of the velocity fluctuations to the mean flow velocity. A turbulence intensity of 1 % or less is generally considered low and turbulence intensities greater than 10% are considered high. Turbulence intensity was selected 5 % and 10%, respectively for inlet and outlet zone. The turbulent viscosity ratio is directly proportional to the turbulent Reynolds number. At the free stream boundaries of most internal flows turbulent viscosity ratio is fairly small. Typically, the turbulence

parameters were set between 1 to 10. Turbulent viscosity ratio was selected 5 and 10, respectively for inlet and outlet zone in the present numerical study.

3.7 Operating Conditions

Operating pressure is significant for low-Mach-number compressible flows because of its role in avoiding round off error problems Operating pressure is less significant for higher-Mach number compressible flows. The pressure changes in such flows are much larger than those in low-Mach-number compressible flows, so there is no real problem with round off error and there is no real need to use gauge pressure. The criteria for choosing a suitable operating pressure are based on the Mach-number regime of the flow and the relationship that is used to determine density. Due transonic regime and density according to ideal gas law operating pressure was set to zero.

3.8 Monitoring Solution Convergence

At the end of each solver iteration, the residual sum for each of the conserved variables is computed and stored, thus recording the convergence history. This history is also saved in the data file. On a computer with infinite precision, these residuals will go to zero as the solution converges. On an actual computer, the residuals decay to some small value and then stop changing. For the present case all residual value was set to 0.00001 for continuity, x velocity, y velocity, energy, turbulent kinetic energy and specific dissipation rate.

3.9 Computational Conditions:

Fig. 3.1-3.7 shows the details of test section. Chord length *c* of the circular arc airfoil is 48 mm. The leading edge and tailing of the airfoil is kept sharp. The thickness t and the radius of the circular arc *R* are 0.15*c* and 1.7*c*, respectively. Computational domain is discretized by structured mesh with (360 x 80) + (110 x 100) = 39800 grid. The minimum normal grid spacing was reduced to 8.34 x 10^{-5} chords, ensuring a value of y^+ <3 everywhere on the airfoil surface. The origin of (x, y) coordinate is located at leading edge of the airfoil. The airfoil is kept at zero angle of attack. The pressure ratio p/p_{in}, where p is total outlet pressure and p_{in} inlet pressure, was varied from 0.71 to 0.75. The inlet Mach numbers upstream of the airfoil are 0.61, 0.61, 0.61, 0.61, and 0.61 for p/p_{in} =0.71, 0.72, 0.73, 0.74, and 0.75 respectively. The following computational conditions were set up for the computational analysis:

At atmospheric conditions, T_∞ =300k, p_{in} =101325 Pa,

For air, ρ=1.176674 kg/m^3, μ= 1.7894×10^{-5} N.s/m^2, v_∞=211.724m/s for M_∞=0.61, c=0.048m. Re=6.68×10^5

CHAPTER 5

CONTROL OF SHOCK OSCILLATIONS

5.1 Shock control

In order to control self-induced shock wave a passive control technique 'Shock Control Cavity' is drawn in a preprocessing tool and observed the shock wave dynamics on biconvex airfoil numerically. The airfoil with a cavity with a cavity deep to 2% of aerofoil chord, cavity length is 5% of airfoil chord is shown in figure-5.1. The cavity located at the mean shock position (peak root means square position) on the aerofoil.

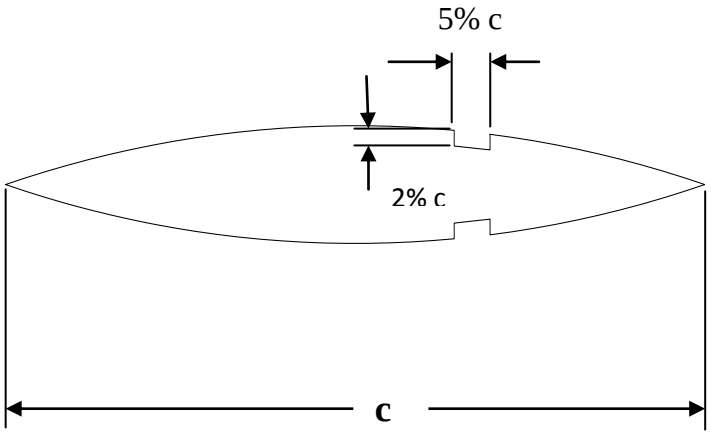

Figure 5.1: Cavity geometry on airfoil with parameters

Following table 5.1 shows the cavity location on airfoil for different pressure ratio.

Table 5.1: Location, Length and height of cavity with different pressure ratio

Pressure Ratio	Location of cavity in (%) of chord	Length of cavity in (%) of chord			Height of cavity in (%) of chord
0.71	71	5			2
0.72	71	5	7	10	2
0.73	70	5			2
0.74	68	5			2
0.75	67	5			2

In order to control shock wave around circular arc airfoil, a cavity deep to 2% of aerofoil chord, cavity length is 5% of airfoil chord introduced at the mean shock position (peak root means square position) on the aerofoil for pressure ratio range 0.71-0.75. To observe the effect of cavity size on shock wave dynamics, the cavity of cavity length 7% of airfoil chord and 10% of airfoil chord with same height is then introduced at the mean shock position for the pressure ratio of 0.72.

5.1.1 Mach contour with cavity with cavity length 5% of chord

To control self-sustained shock oscillation around biconvex airfoil cavity is introduced and observed its effectiveness.

To control self-sustained shock oscillation around biconvex airfoil for *PR*=0.71 a cavity is created at *x/c*=0.68-0.73 as mean shock was found at *x/c*=0.71. Steady shock wave on upper surface and lower surface of airfoil is observed at the same position as shown in figure 5.2.

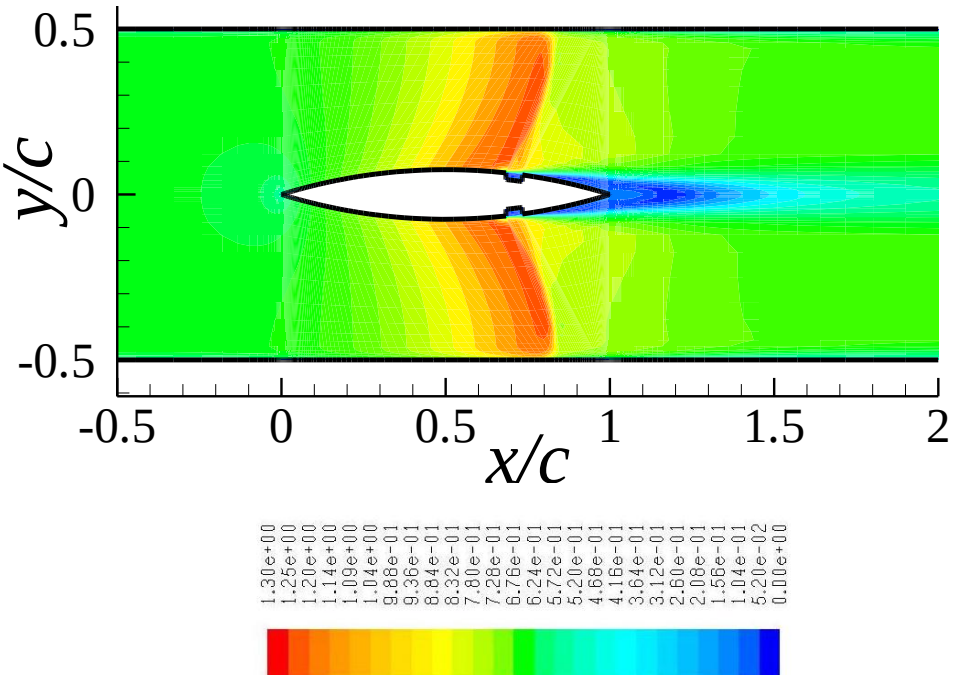

Figure 5.2: Contour maps of Mach number with cavity for *PR*=0.71

For *PR*=0.72 a cavity is created at *x/c*=0.68-0.73 as mean shock was found at *x/c*=0.71. Fig. 5.3 shows sequential contour maps of Mach number at *PR*=0.72 with cavity during one cycle at time step of 1/10*f*. The upstream shock movement has been observed within *x/c*=0.60 to 0.85. The shock wave appeared both upper surface and lower surface of the airfoil during the cycle.

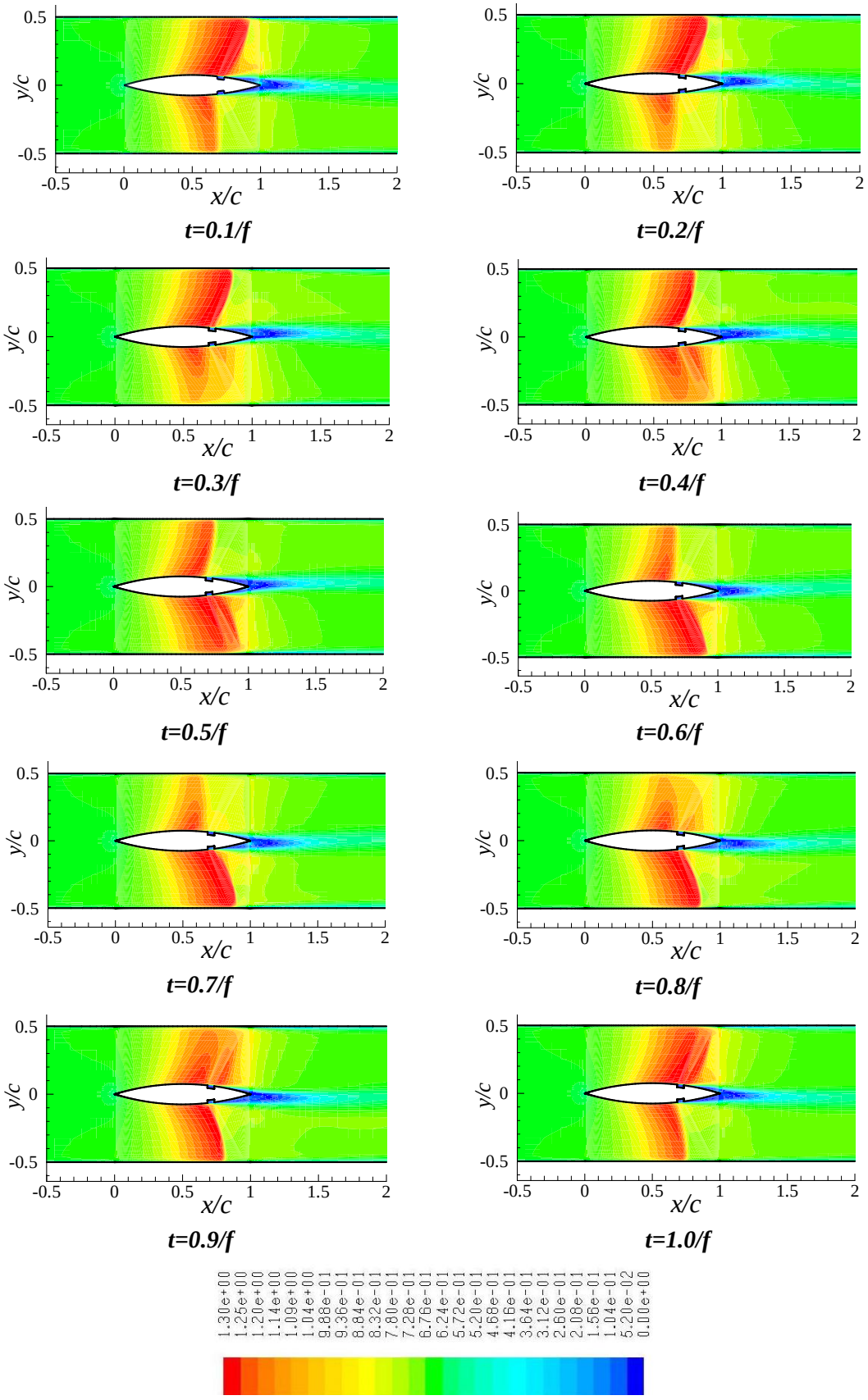

Figure 5.3: Sequential contour maps of Mach number with cavity during one cycle for *PR*=0.72

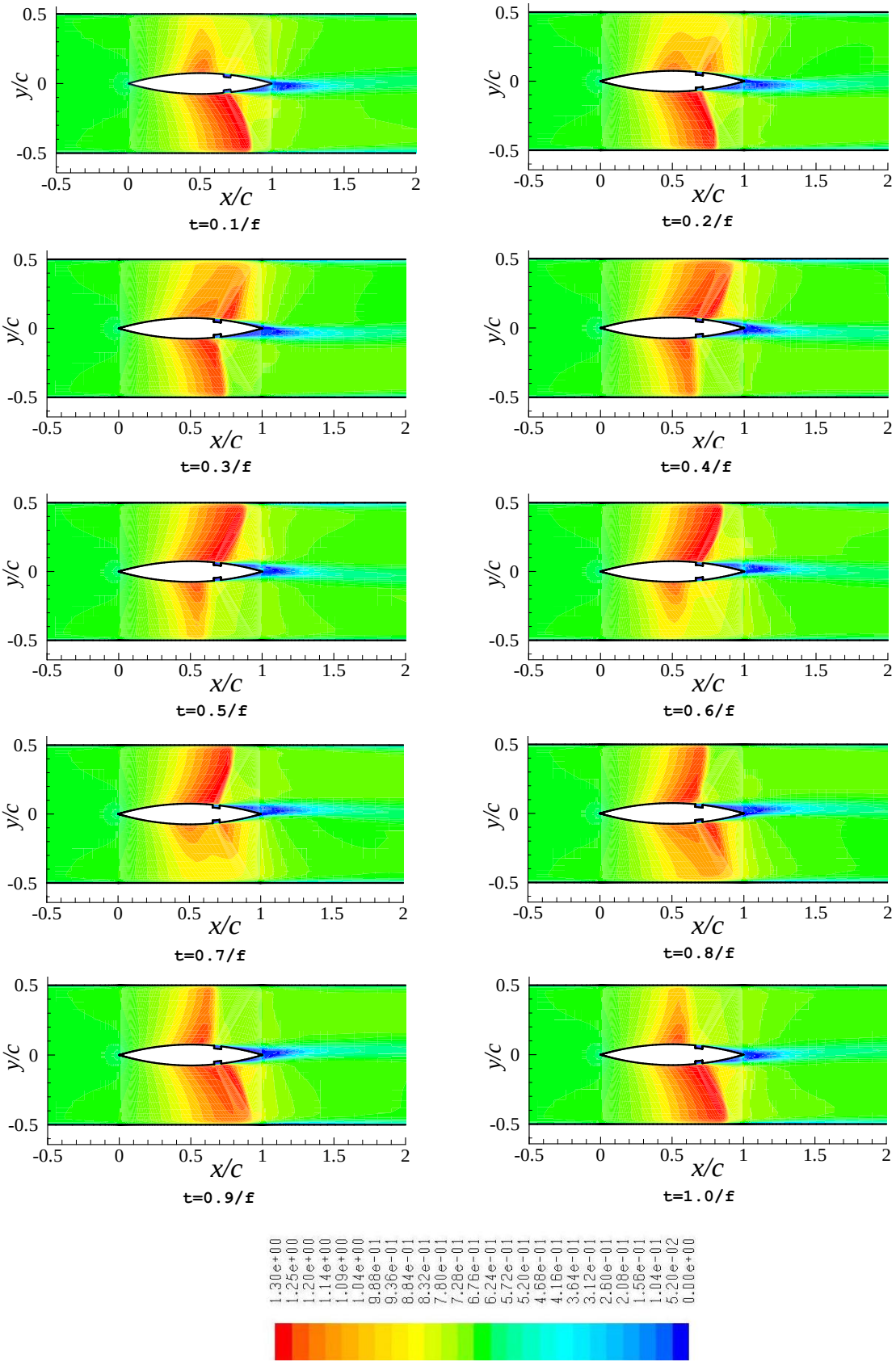

Figure 5.4: Sequential contour maps of Mach number with cavity during one cycle for *PR*=0.73

To control shock wave for *PR=0.73* (fig. 5.4) with similar cavity shape and size positioned at *x/c=0.68-0.72* as mean shock was found *x/c=0.70* and the upstream movement of shock is observed in the range of x/c= 0.60-0.80. Moreover, shock waves are present around the upper and lower surfaces at six time steps of the cycle which was the four time steps at on without cavity model.

During *PR=0.74* (fig. 5.5) similar cavity was positioned at *x/c=0.66-0.71* as mean shock was found at *x/c=0.68.* The upstream movement of shock is observed in the range of x/c= 0.60-0.70, which was in the range of x/c= 0.60-0.80 at on without cavity model.

For *PR=0.75* (fig. 5.6) similar cavity was positioned also at *x/c=0.64-0.69* as mean shock was found at *x/c=0.67.* The upstream movement of shock is observed in the range of *x/c*= 0.65-0.70, which was in the range of *x/c*= 0.60-0.71 at on without cavity model.

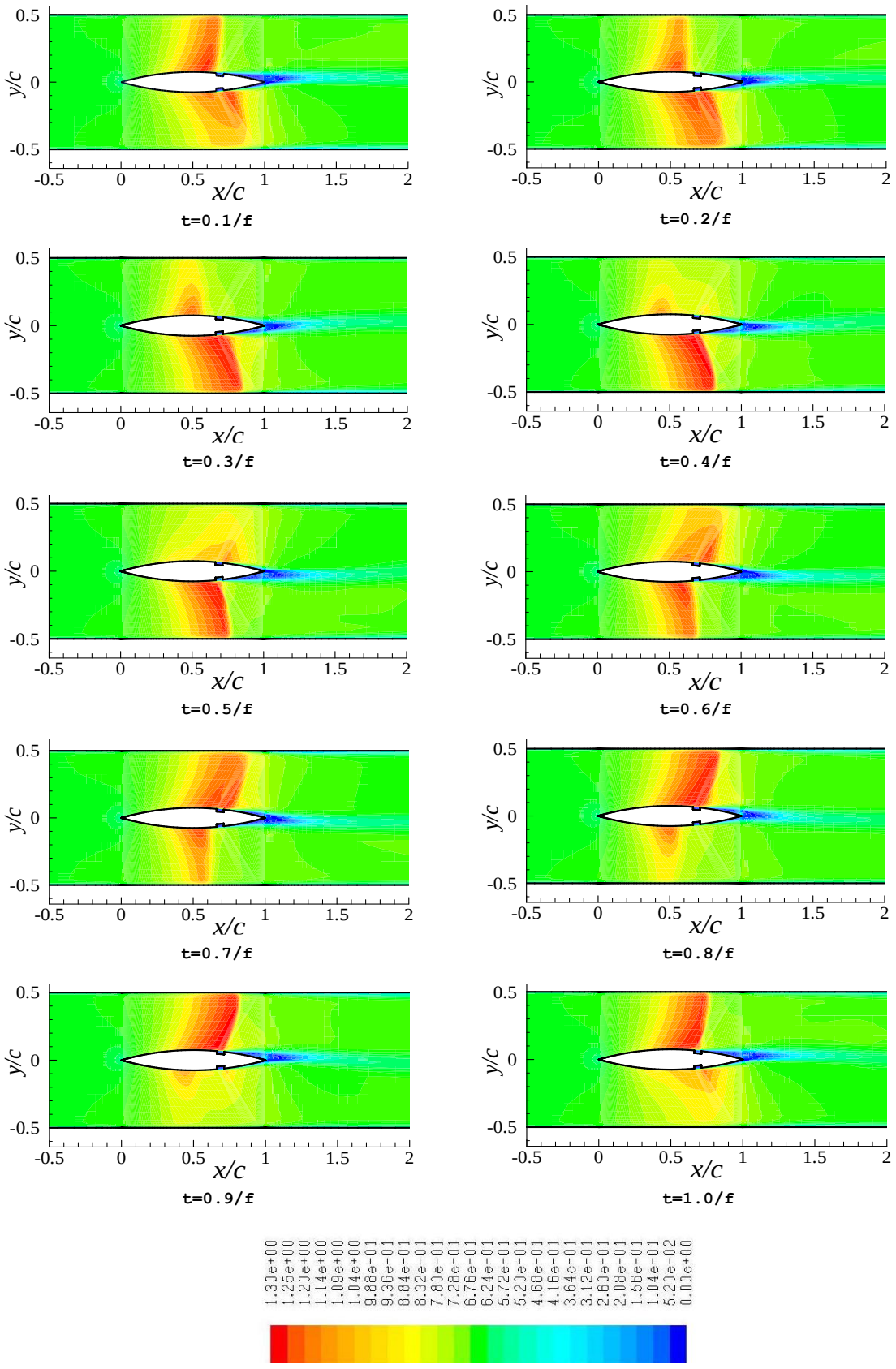

Figure 5.5: Sequential contour maps of Mach number with cavity during one cycle for *PR*=0.74

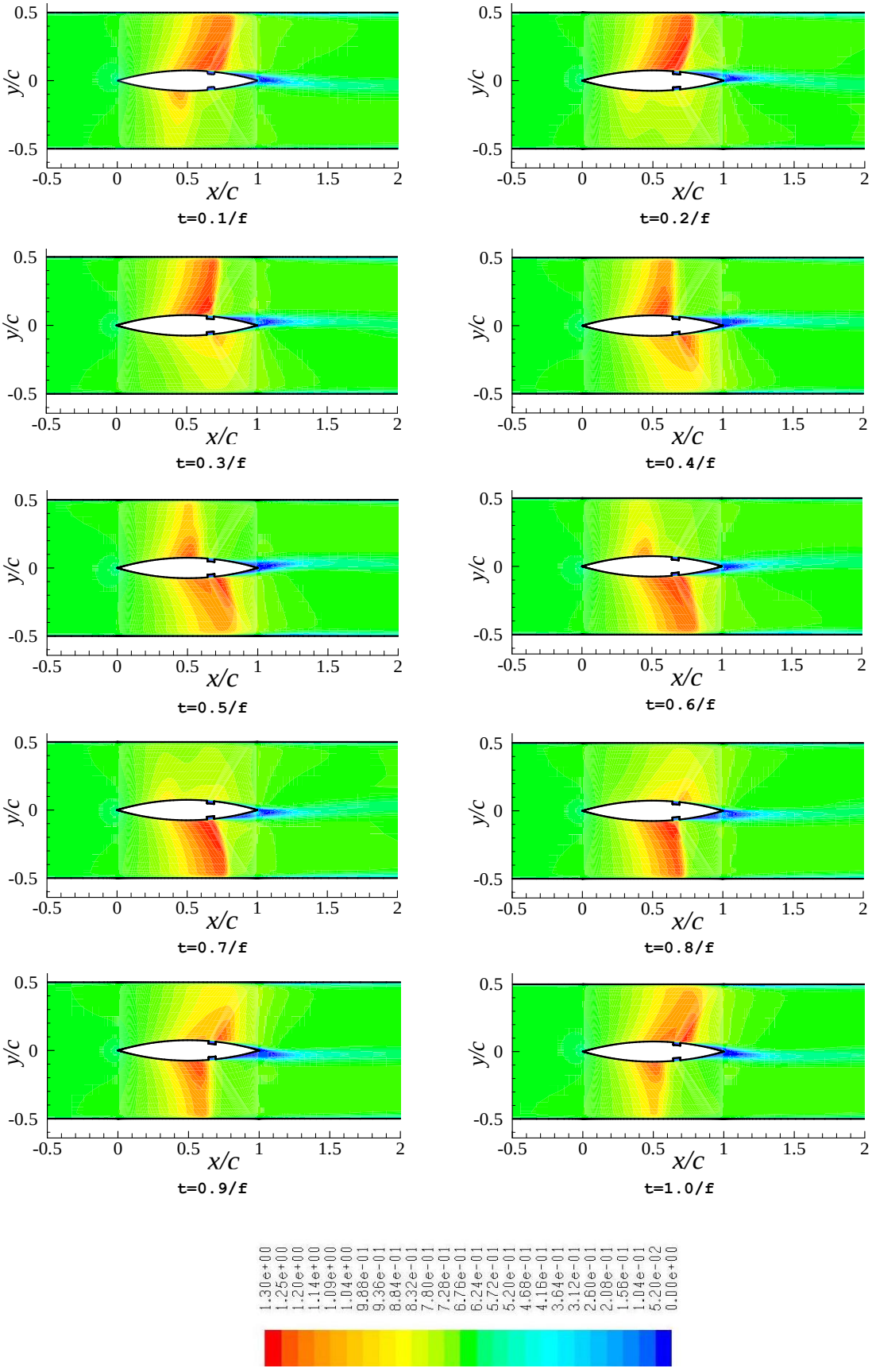

Figure 5.6: Sequential contour maps of Mach number with cavity during one cycle for *PR*=0.75

5.1.2 Mach contour with cavity with cavity length 7% of chord

For *PR*=0.72 a cavity with cavity length 7% chord is created at *x/c*=0.67-0.74 as mean shock was found at *x/c*=0.71. Fig. 5.7 shows sequential contour maps of Mach number at *PR*=0.72 with cavity with cavity length 7% chord during one cycle at time step of 1/10*f*. The upstream shock movement has been observed within *x/c*=0.66 to 0.74, which was in the range of *x/c*= 0.67-0.85 at on cavity with cavity length 5% of chord and in the range of *x/c*= 0.60-0.90 at on without cavity model.

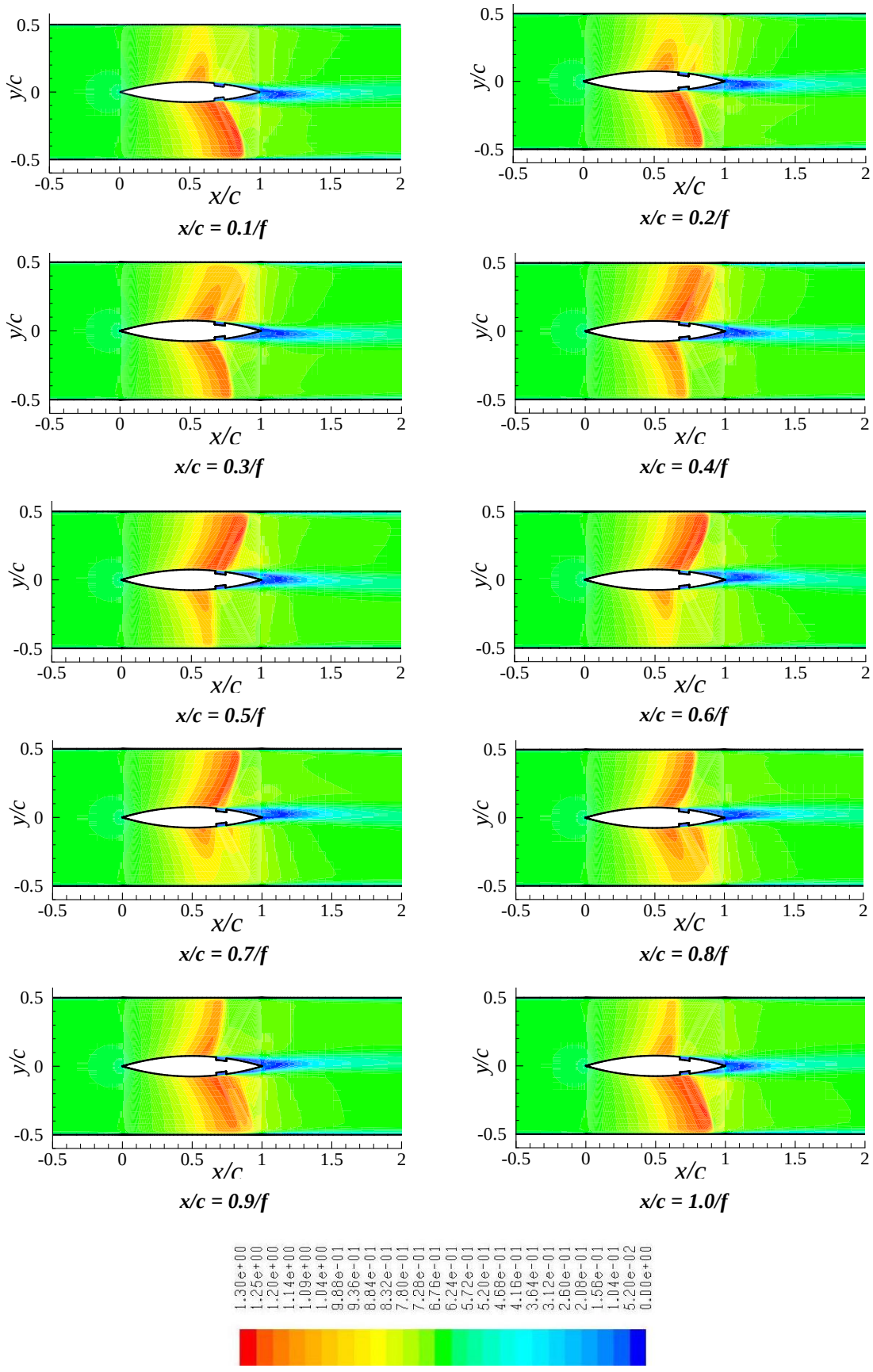

Figure 5.7: Sequential contour maps of Mach number with cavity with cavity length 7% of chord during one cycle for *PR*=0.72

5.1.3 Mach contour with cavity with cavity length 10% of chord

For *PR*=0.72 a cavity with cavity length 10% chord is created at *x/c*=0.658-0.758 as mean shock was found at *x/c*=0.71. Fig. 5.8 shows sequential contour maps of Mach number at *PR*=0.72 with cavity with cavity length 10% chord. The shock waves oscillate alternately between upper and lower surfaces within *x/c*=0.658 to 0.70, which was in the range of *x/c*= 0.66-0.74, *x/c*= 0.67-0.85 and *x/c*= 0.60-0.90 at on cavity with cavity length 5% of chord, cavity with cavity length 7% of chord and without cavity model respectively. In that case the Tijdeman type C shock oscillation is changed to Tijdeman type A shock oscillation.

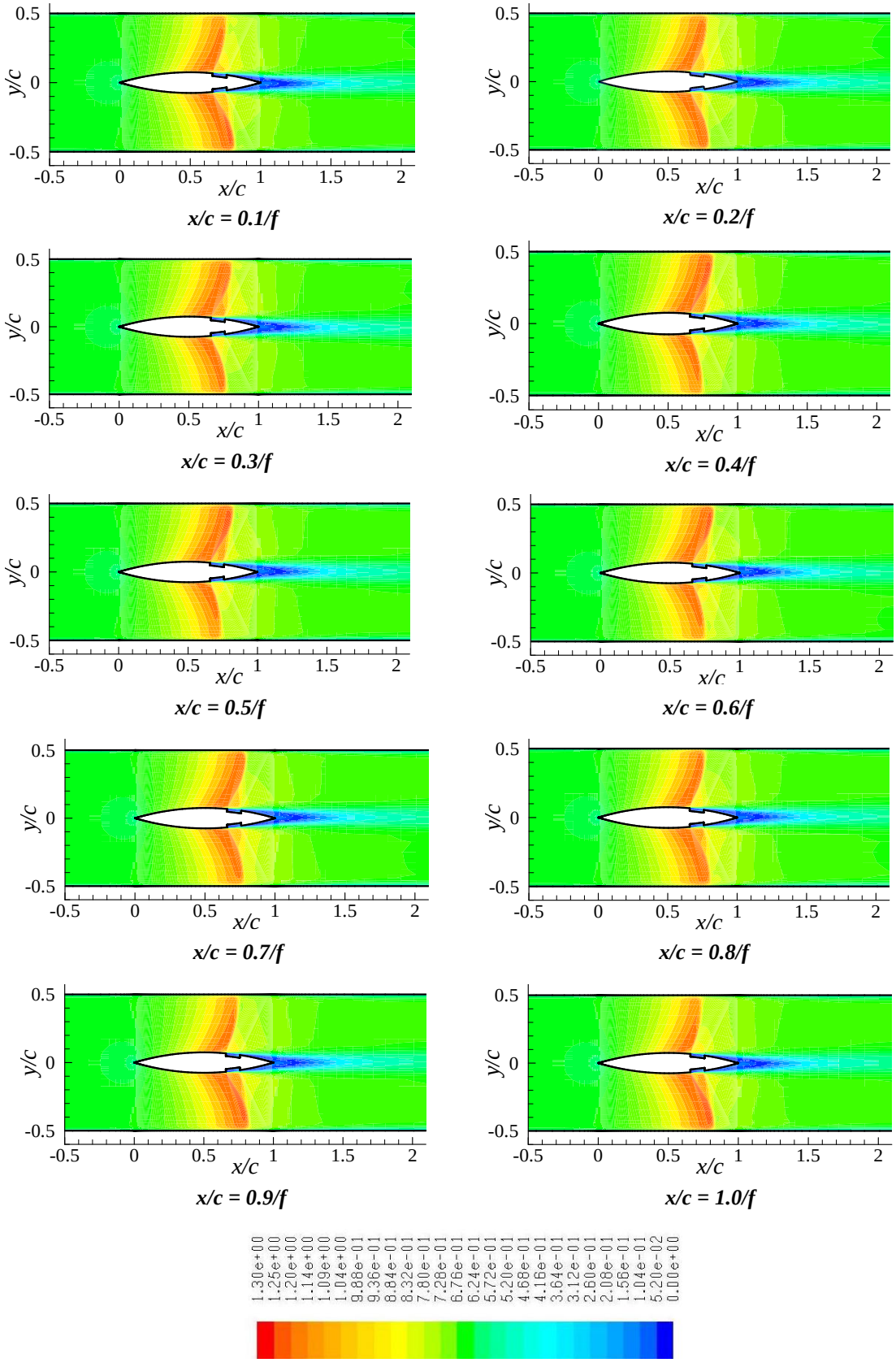

Figure 5.8: Sequential contour maps of Mach number with cavity with cavity length 10% of chord during one cycle for *PR*=0.72

5.1.4 Static Pressure-time history

Figure 5.9 to 5.13 shows static pressure-time histories in the flow field around an airfoil with cavity with cavity length 5% chord at different point on airfoil surfaces with. Steady pressure oscillation is observed for pressure ratio of 0.71 which indicates that the shock induced oscillation has been stopped for the exciting flow condition by cavity insertion. At *PR*=0.72-0.75, unsteady shock wave is observed but the pressure oscillation has been reduced

Figure 5.14 shows static pressure-time histories in the flow field around an airfoil with cavity with cavity length 5% chord, 7% chord and 10% chord at different point on airfoil surfaces only for *PR*=0.72. The static pressure-time histories shows that the shock strength reduced significantly with increasing cavity length from 5% chord to 10% chord and shock frequency increased for cavity length 5% chord then reduced for cavity length 7% chord and 10% chord as shown in Table-5.2.

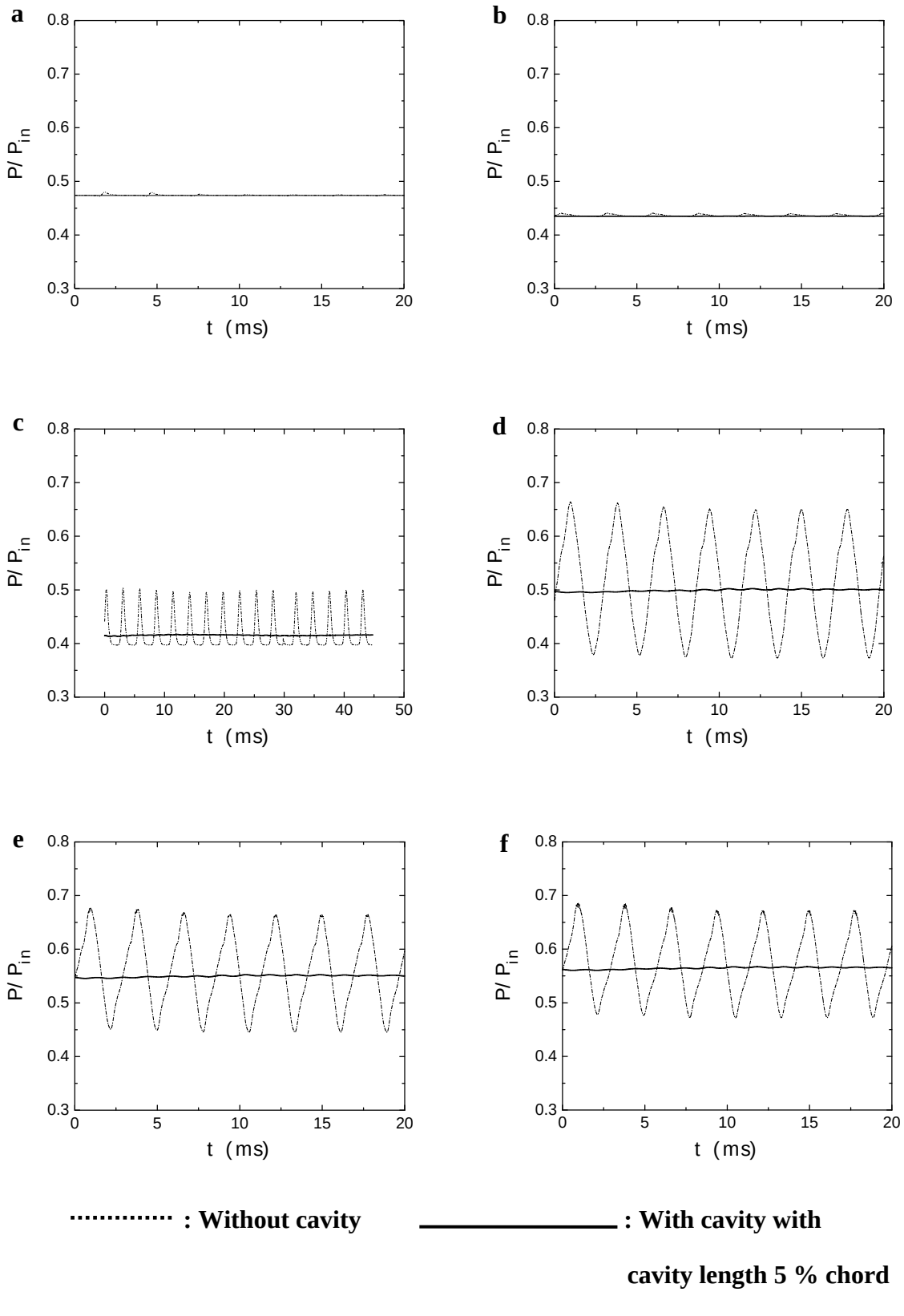

Figure 5.9: Static pressure-time histories in the flow field around an airfoil for *PR*=0.71 at different point on airfoil surface; (a) *x/c*=0.50, (b) *x/c*=0.563, (c) *x/c*=0.625, (d) *x/c*=0.750, (e) *x/c*=0.812, (f) *x/c*=0.875.

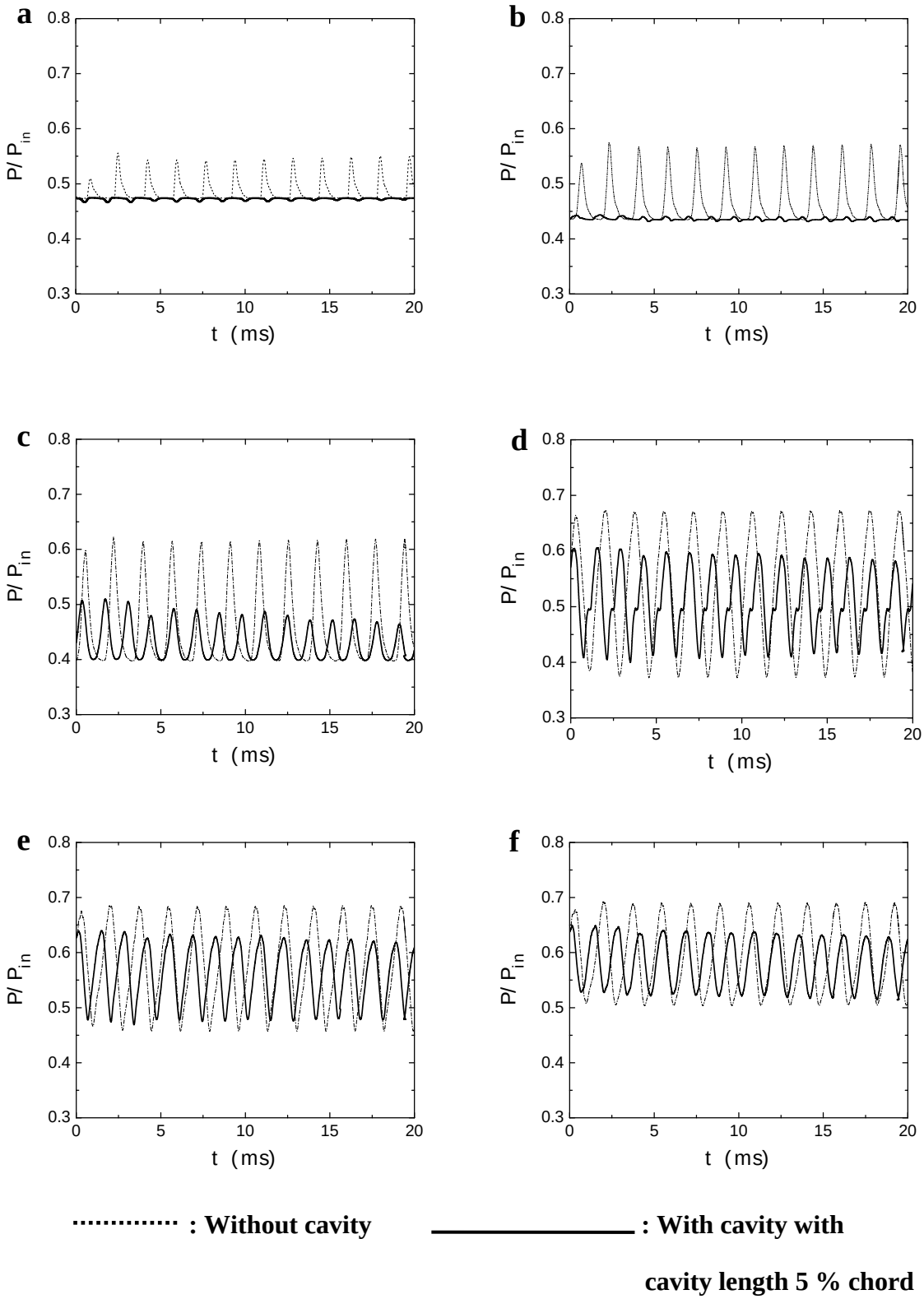

Figure 5.10: Static pressure-time histories in the flow field around an airfoil for *PR*=0.72 at different point on airfoil surface; (a) *x/c*=0.50, (b) *x/c*=0.563, (c) *x/c*=0.625, (d) *x/c*=0.750, (e) *x/c*=0.812, (f) *x/c*=0.875.

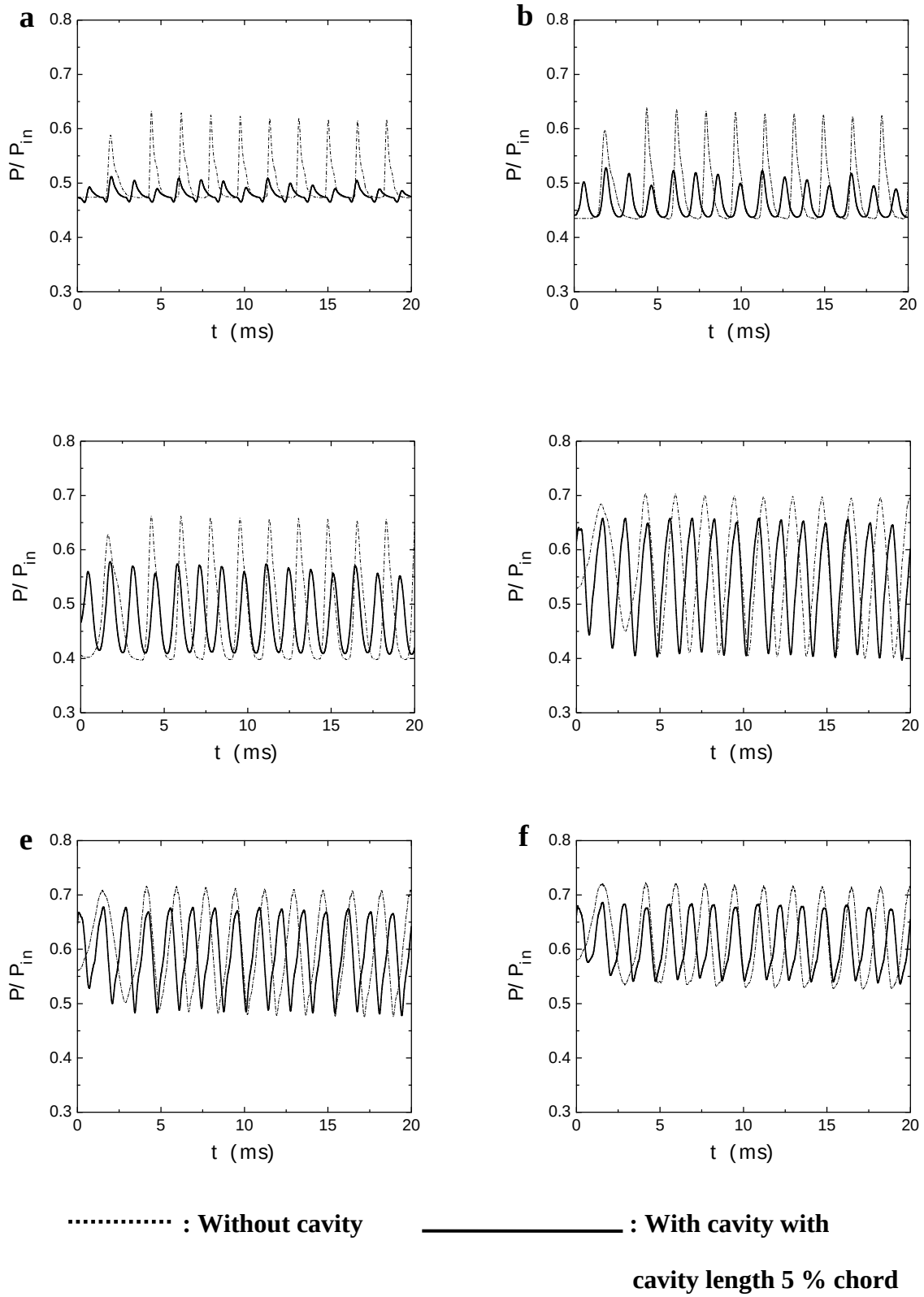

Figure 5.11: Static pressure-time histories in the flow field around an airfoil for *PR*=0.73 at different point on airfoil surface; (a) *x/c*=0.50, (b) *x/c*=0.563, (c) *x/c*=0.625, (d) *x/c*=0.750, (e) *x/c*=0.812, (f) *x/c*=0.875.

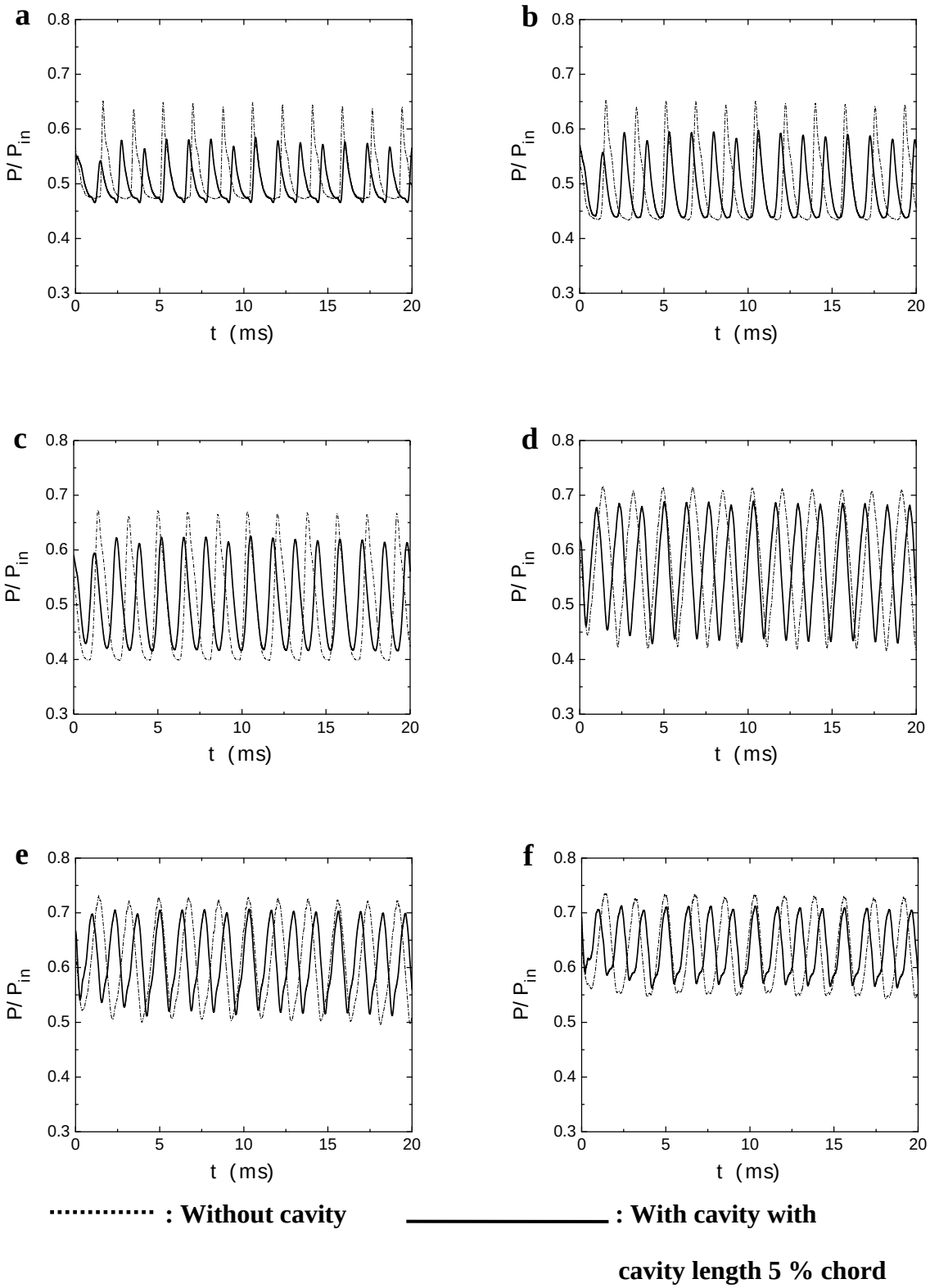

Figure 5.12: Static pressure-time histories in the flow field around an airfoil for *PR*=0.74 at different point on airfoil surface; (a) *x/c*=0.50, (b) *x/c*=0.563, (c) *x/c*=0.625, (d) *x/c*=0.750, (e) *x/c*=0.812, (f) *x/c*=0.875.

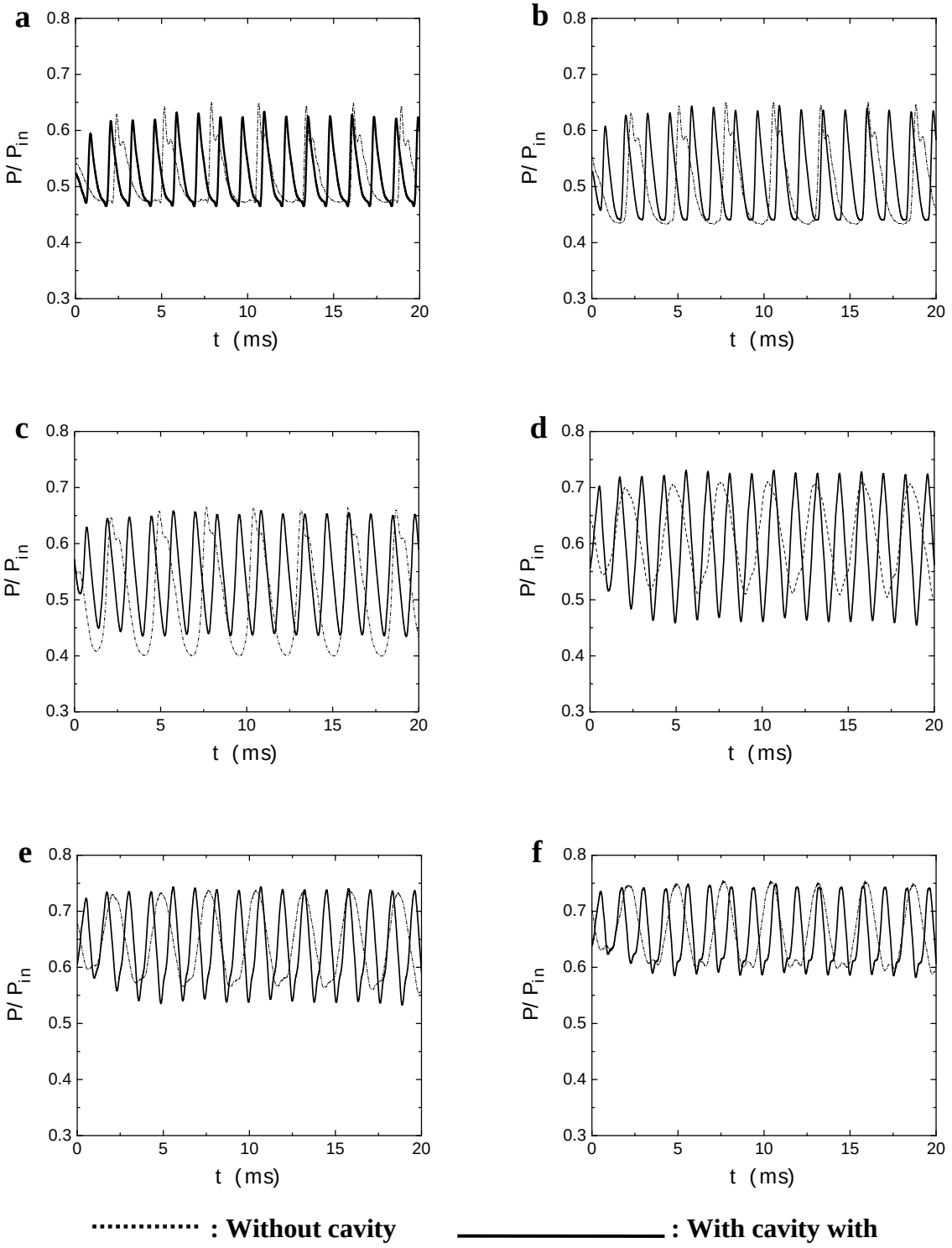

Figure 5.13: Static pressure-time histories in the flow field around an airfoil for *PR*=0.75 at different point on airfoil surface; (a) *x/c*=0.50, (b) *x/c*=0.563, (c) *x/c*=0.625, (d) *x/c*=0.750, (e) *x/c*=0.812, (f) *x/c*=0.875.

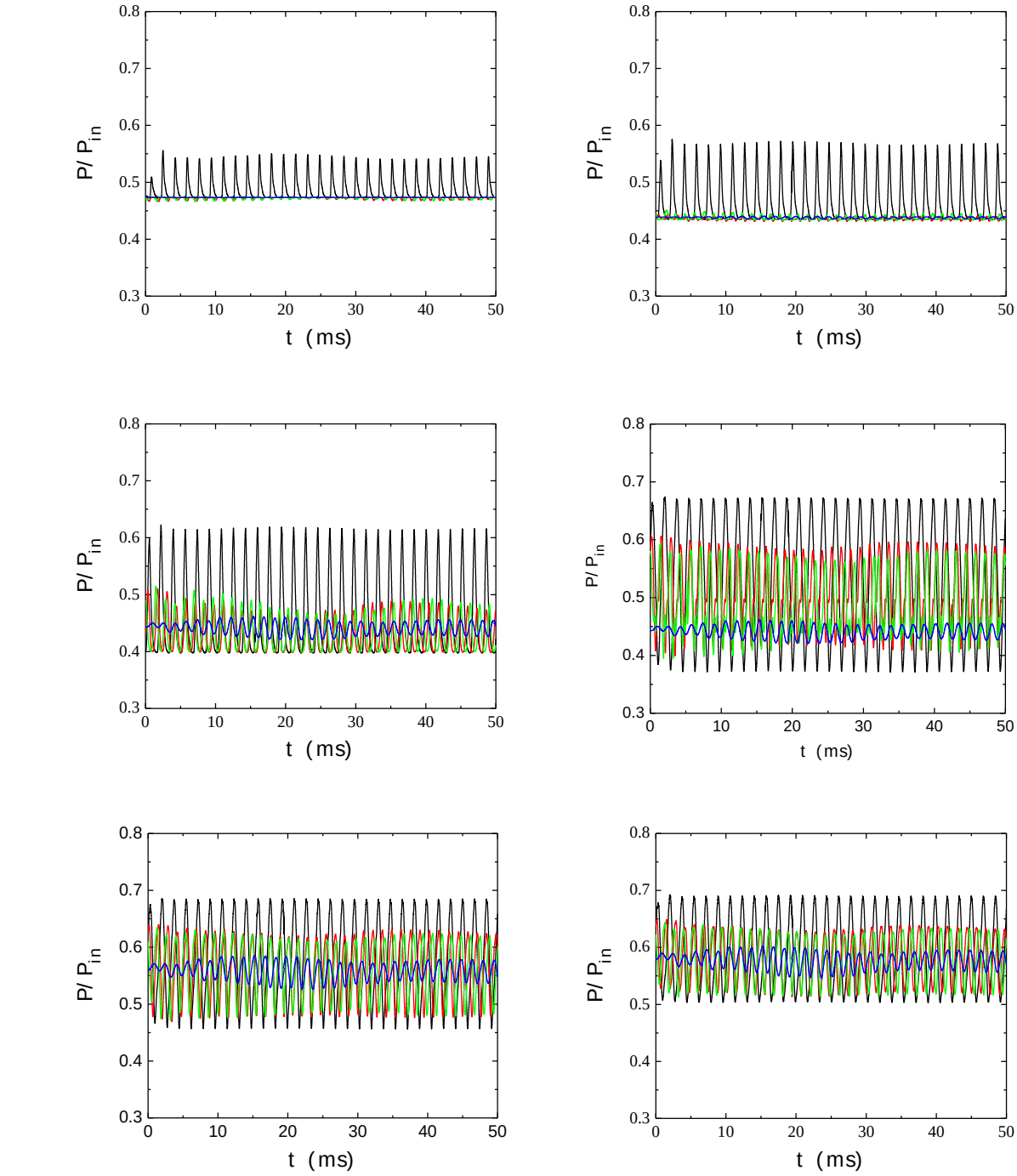

Figure 5.14: Static pressure-time histories in the flow field around an airfoil for *PR*=0.72 at different point on airfoil surface; (a) *x/c*=0.50, (b) *x/c*=0.563, (c) *x/c*=0.625, (d) *x/c*=0.750, (e) *x/c*=0.812, (f) *x/c*=0.875.

5.1.5 Root Mean Square of Pressure Oscillation

Flow field aerodynamic instability around the circular arc airfoil can conveniently be explained by the distribution of root mean square (RMS) value of pressure oscillation induced by shock oscillation. Figure 5.15 shows the distribution of RMS value of pressure oscillation p_{rms}/q_0 (p_{rms}: RMS of pressure oscillation; q_0: dynamic pressure) around upper passage of the airfoil. The values of p_{rms}/q_0 begins to increase from the leading edge of the airfoil and the peak is observed at the location of shock oscillation. In case of without cavity, the peak RMS values are 0.45 for *PR*=0.71, 0.46 for *PR*=0.72, 0.48 for *PR*=0.73, 0.48 for *PR*=0.74, and 0.40 for *PR*=0.75 respectively. Whereas in case of with cavity with cavity length 5% of chord, the peak RMS values are 0.014 for *PR*=0.71, 0.28 for *PR*=0.72, 0.36 for *PR*=0.73, 0.36 for *PR*=0.74, and 0.37 for *PR*=0.75 respectively. Which shown that the shock strength reduced by introducing cavity as a passive means of shock control. With cavity model, the RMS values of pressure oscillation are negligible for pressure ratio 0.71 and very small over the airfoil surface for the pressure ratio 0.72 to 0.74. The RMS values of pressure oscillation are very small in the range of *x*/*c* = 0 to 0.7 compared to without cavity model. The results also show that with the cavity the frequency of shock motion, as shown in Table 5.2, is increased and the mean shock position has moved from *x/c*=0.70 to *x/c*= 0.75 for *PR*=0.73, *x/c*=0.70 to *x/c*= 0.75 for *PR*=0.74, *x/c*=0.65 to *x/c*= 0.75 for *PR*=0.75 and remain unchanged for *PR*=0.71 and 0.72 respectively.

To observe the effect of cavity size on shock wave dynamics, the cavity of cavity length 7% of airfoil chord and 10% of airfoil chord with same height is then introduced at the mean shock position for the pressure ratio of 0.72. Fig. 5.16 shows that the RMS value of

the pressure oscillation reduced significantly from 0.46 to 0.28, 0.26 and then 0.08. In both cases the frequency of shock oscillation reduced also which is shown in Table 5.2.

Table 5.2: Comparison of Frequency of shock oscillation with cavity and without cavity at different pressure ratio

Pressure Ratio (*PR*)	Frequency of shock oscillation without cavity (Hz)	Frequency of shock oscillation with cavity with cavity length 5% of chord (Hz)	Frequency of shock oscillation with cavity with cavity length 7% of chord (Hz)	Frequency of shock oscillation with cavity with cavity length 10% of chord (Hz)	Type of shock without cavity	Type of shock with cavity
0.71	362	-			A	Steady
0.72	600	738	729	637	C	A
0.73	570	745			C	C
0.74	568	760			C	C
0.75	364	800			C	C

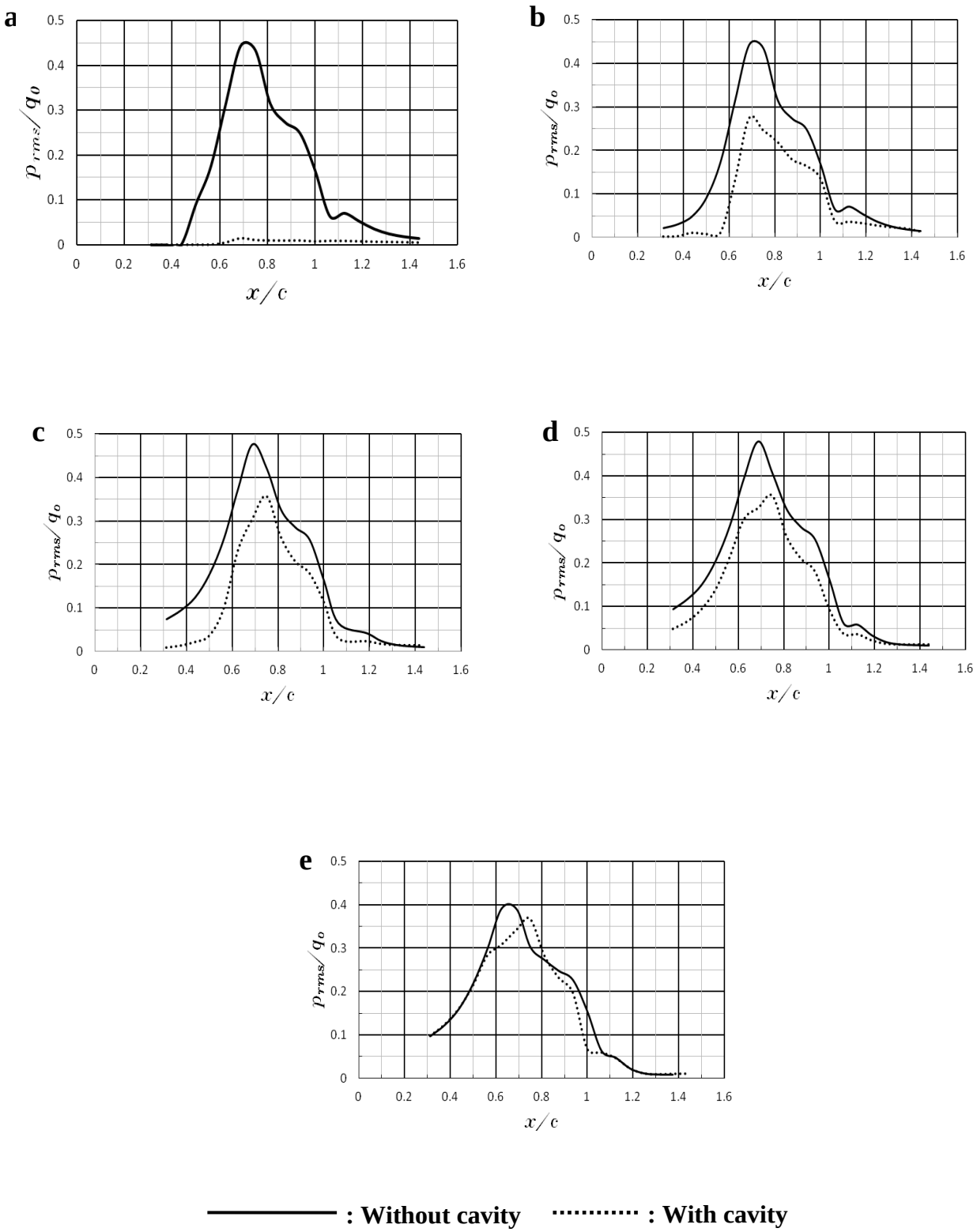

Figure 5.15: Distribution of RMS value of pressure oscillation around a circular arc airfoil;

(a) *PR*=0.71, (b) *PR*=0.72, (c) *PR*=0.73, (d) *PR*=0.74, (e) *PR*=0.75

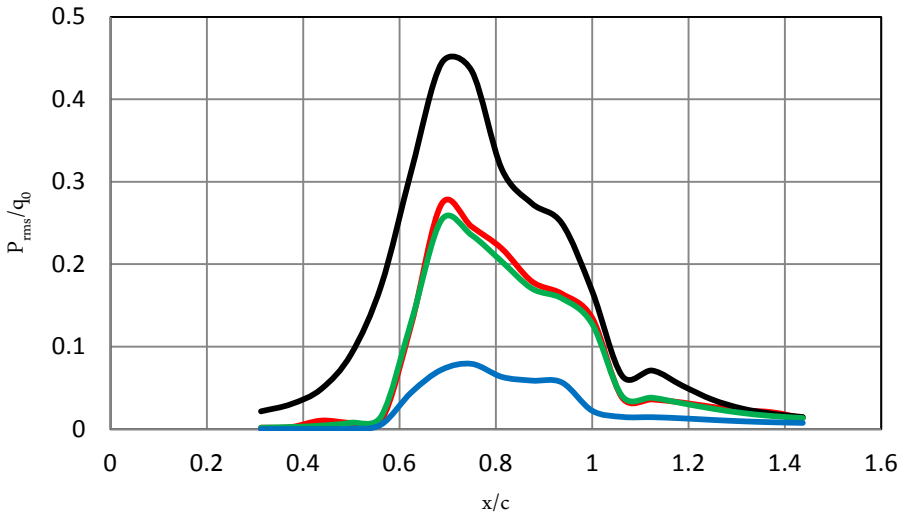

: Without cavity

: Cavity with cavity length 7% of chord

: Cavity with cavity length 5% of chord

: Cavity with cavity length 10% of chord

Figure 5.16: Distribution of RMS value of pressure oscillation around a circular arc airfoil for *PR*=0.72

5.1.6 Turbulent Kinetic Energy distribution

Figure 5.17-5.21 shown the contour of distribution of Turbulent kinetic energy during a cycle at time step of 1/10*f* for *PR*=0.71, 0.72, 0.73, 0.74, and 0.75 respectively. *f* is the shock induced oscillation (SIO) frequency at the position of peak RMS value of pressure oscillation. Dark region in the contour represent maximum turbulent kinetic energy. The dimension less turbulent kinetic energy ($\frac{k}{v_\infty^2}$) observed in the range of 0.097-0.80 for *PR*=0.72, 0.088-0.074 for *PR*=0.73, 0.084-0.07 for *PR*=0.74 and 0.080-0.062 for *PR*=0.75 respectively. Steady turbulent kinetic energy distribution observed for *PR*=0.71 and turbulent kinetic energy reduced 10%.

Maximum turbulent kinetic energy observed at time step of *t=0.3/f* and *0.8/f* for *PR=0.72, t=0.1/f* and *t=0.6/f* for *PR=0.73, t=0.2/f* and *t=0.7/f* for *PR=0.74, t=0.1/f* and *t=0.6/f* for *PR=0.75* respectively. The strong shock wave appeared both side of airfoil as compare to the other time steps of the cycle. The dimension less turbulent kinetic energy ($\frac{k}{v_\infty^2}$) observed 10% less as compared to the without control.

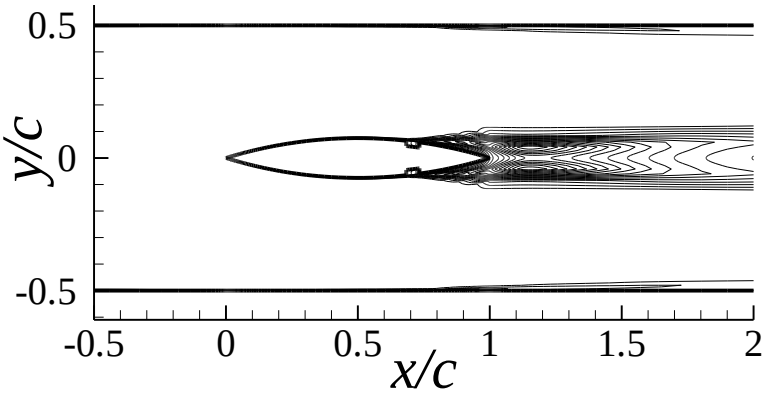

Figure 5.17: Contour of distribution of Turbulent kinetic energy with cavity during a cycle for *PR*=0.71

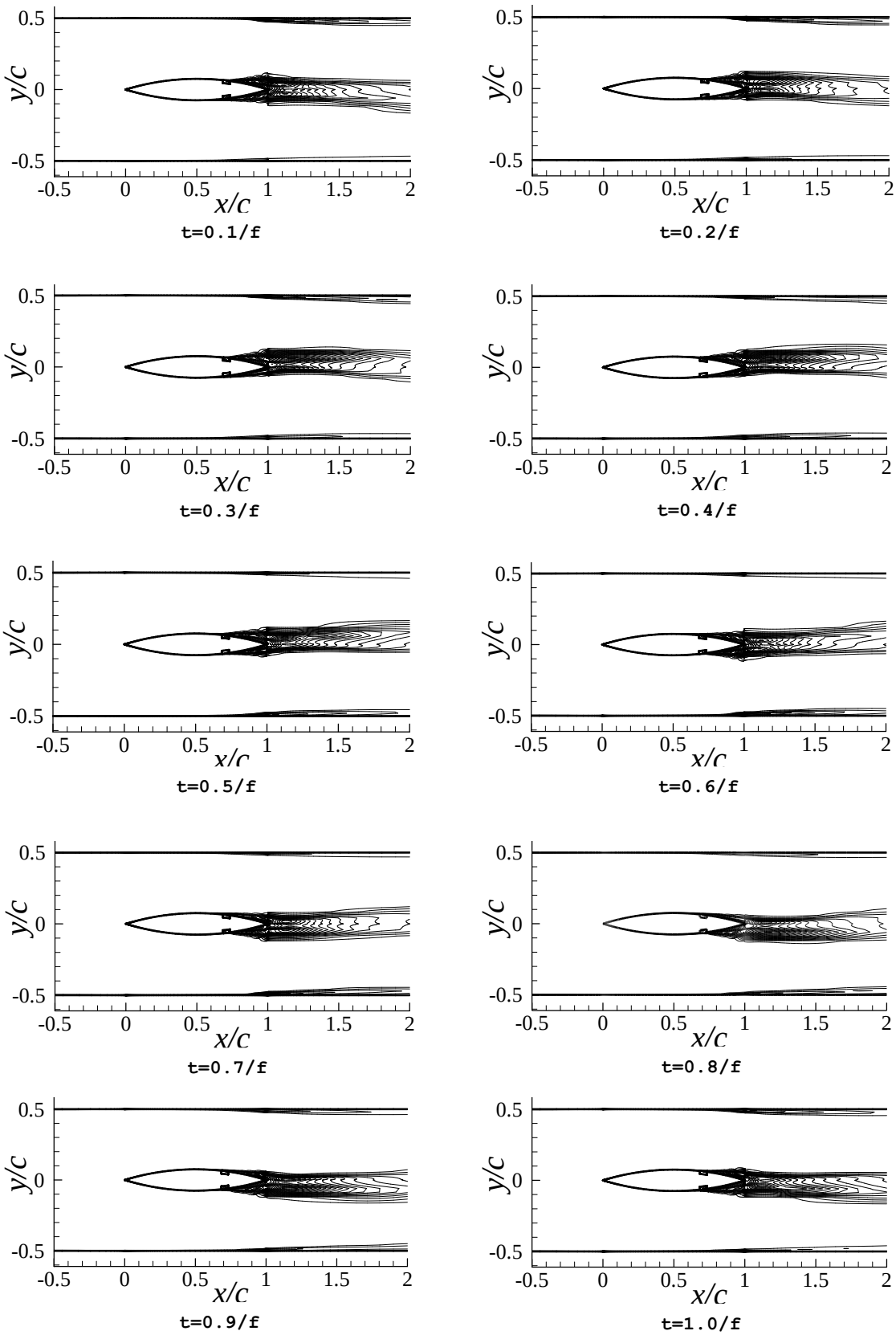

Figure 5.18: Contour of distribution of Turbulent kinetic energy with cavity during a cycle for *PR*=0.72

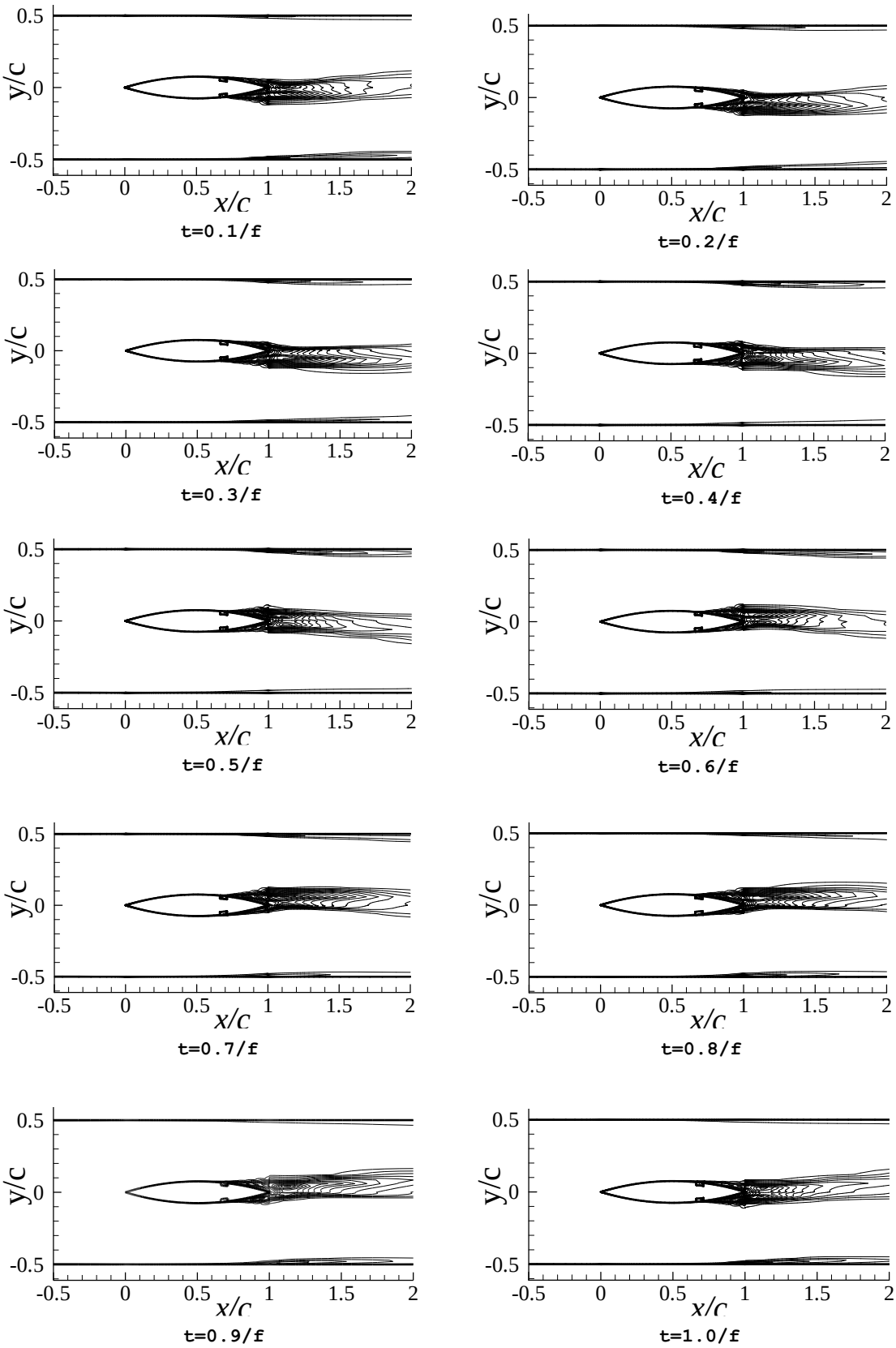

Figure 5.19: Contour of distribution of Turbulent kinetic energy with cavity during a cycle for *PR*=0.73

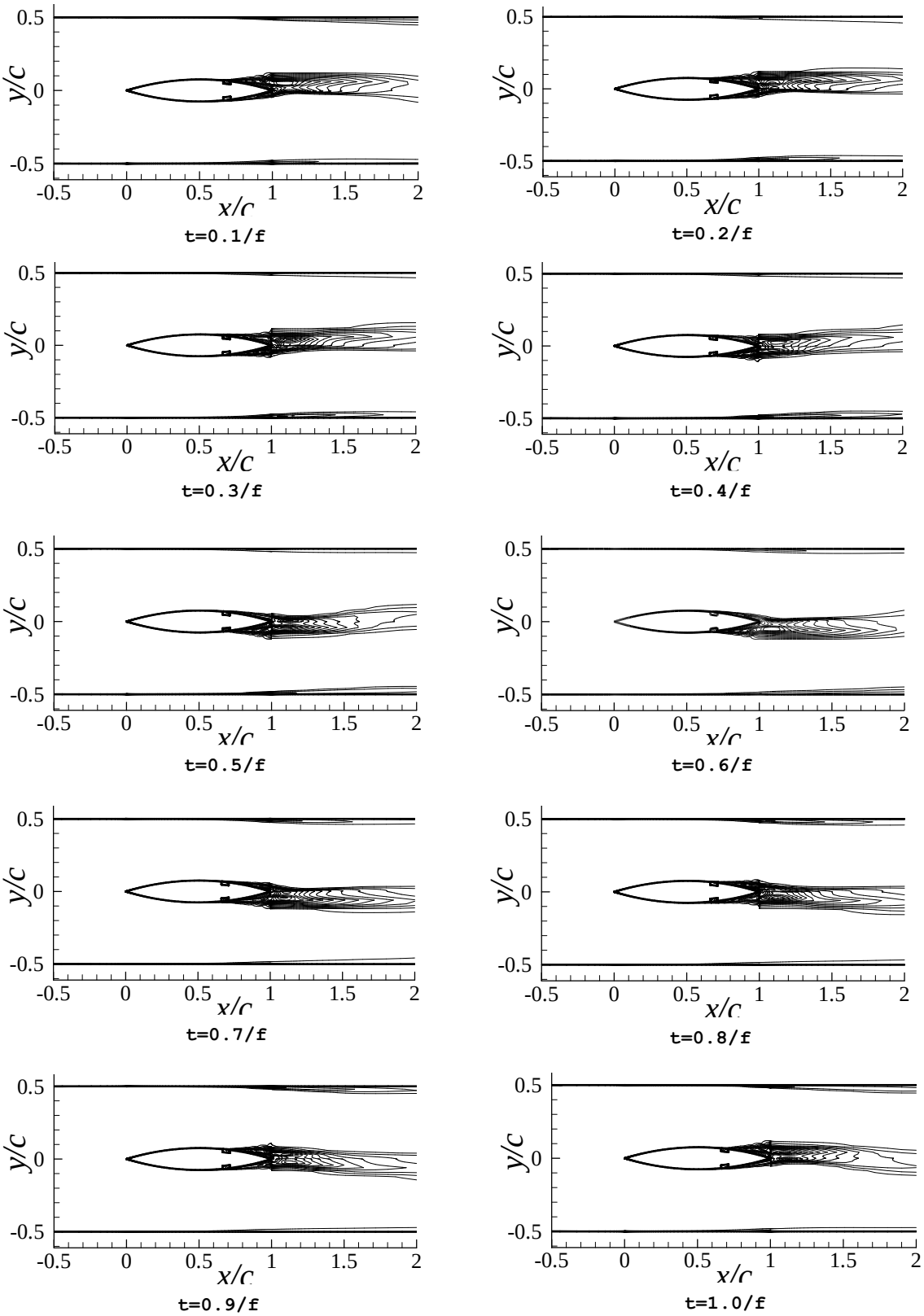

Figure 5.20: Contour of distribution of Turbulent kinetic energy with cavity during a cycle for *PR*=0.74

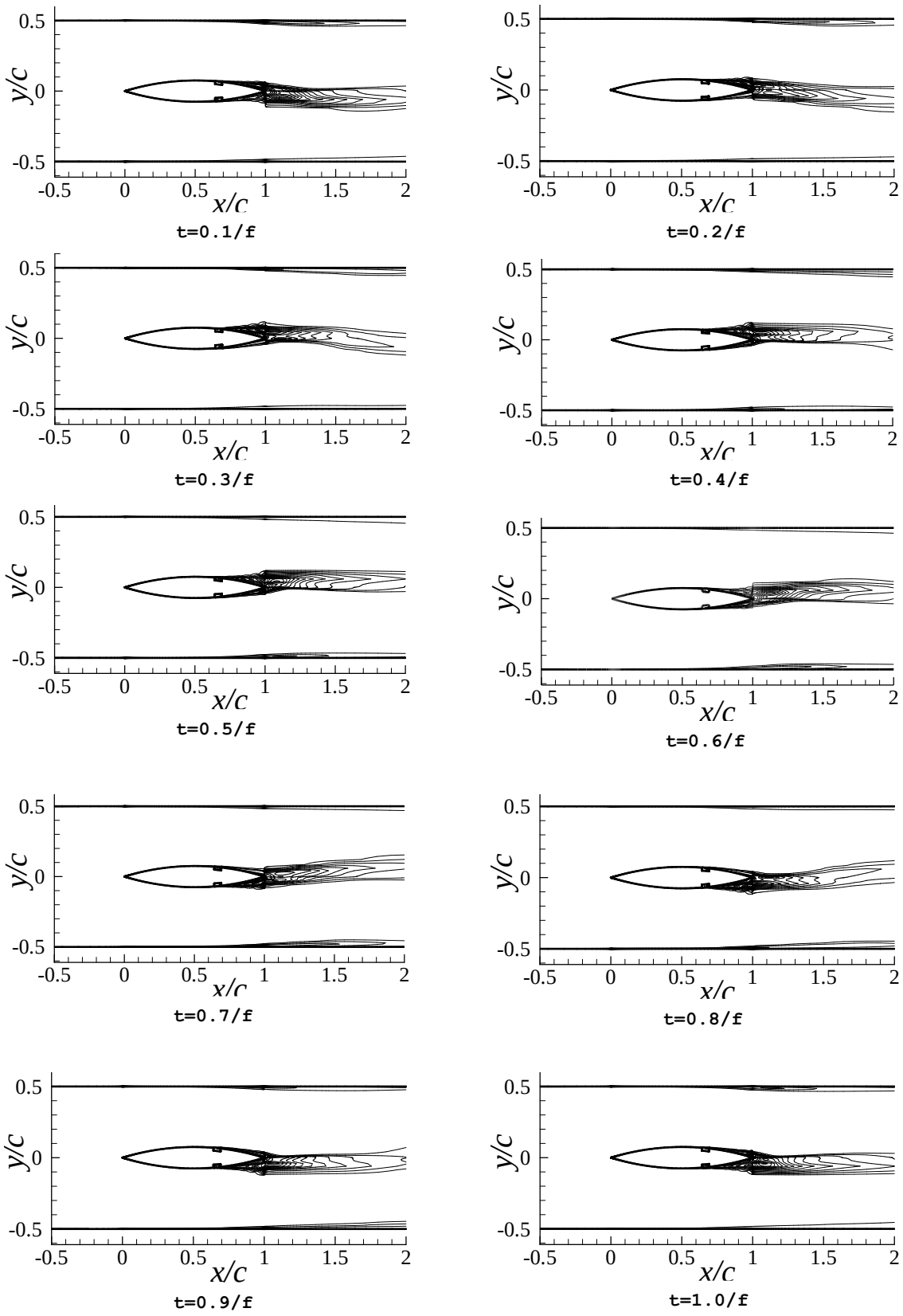

Figure 5.21: Contour of distribution of Turbulent kinetic energy with cavity during a cycle for *PR*=0.75

CHAPTER 6

CONCLUSION AND FUTURE SCOPE OF RESEARCH

6.1 Conclusion

In the present study the numerical computation of the self-excited oscillation on the circular arc airfoil in transonic internal flow is conducted using the unsteady compressible Navier-Stokes equations together with the mass conservation equation and the energy equation. Two additional transport equations of k-ω SST turbulence model are included to model the turbulence in the flow field. Since the free stream Mach number of the present problem is in the range of 0.6 to 0.64, a density based solver is used. A second-order upwind scheme for the discretization of flow and turbulence equations is used. For time integration, a second order implicit scheme is used. The computational domain is discretized into a structured mesh. The total pressure ratio is varied from 0.71 to 0.75. The present study has given some numerical observations regarding unsteady shock wave phenomena of 15% circular arc airfoil as follows:

1. From observation of Mach contour and Static pressure-time histories it is found that the shock waves oscillate alternately between upper and lower surfaces of airfoil during the cycle (Tijdeman type A) for PR=0.71 and the shock wave moves upstream only between upper and lower surfaces of airfoil during the cycle (Tijdeman type C) for PR=0.72-0.75.
2. Distribution of RMS values of shock induced pressure oscillation around an airfoil shows that the mean shock position moves upstream with increasing pressure ration from 0.71-0.75. The upper and lower surface SIO observed at about 180^0 out of phase.

3. Pressure ratio increment also shows that the shock movement region become narrow with increasesd pressure ratio from 0.71-0.75.
4. It is also observed from turbulent kinetic energy distribution that the turbulent kinetic energy decreases with increases pressure ratio from 0.71 to 0.75.
5. A cavity was introduced as a passive means of shock induced oscillation at mean shock wave position of airfoil to control shock induced oscillation. Numerically observed its effectiveness resulting steady shock for PR=0.71 and shock strength reduction for PR=0.72-0.75.
6. To observe the effect of cavity size on shock wave dynamics, the cavity of cavity length 7% chord and 10% chord is then introduced at the mean shock position for the pressure ratio of 0.72 and significant reduction of both shock strength and shock oscillation observed .

6.2 Future Scope of Research

The following recommendations can be made for future works from experience gained while achieving the set objectives of this thesis:

(1) The present analysis can be extended to on the other types of airfoil.

(2) To get more effective results numerically with similar study, 3D computation can be done.

(3) The numerical simulation can be performed at different angle of attack.

(4) The computation can be performed with other turbulence model like large eddy simulation (LES) and direct numerical simulation (DNS) which is more effective than SST k-ω model.

(5) Different cavity size can be used for controlling of shock wave oscillation.

REFERENCES

[1] Lee, B.H.K., “Self-sustained shock oscillations on airfoils at transonic speeds”, *Progress in Aerospace Sciences*, 37, 147-196, 2001.

[2] Lepicovsky, J., McFarland, E.R., Chima, R.V., Capece, V.R., Hayden, J., "Intermittent flow regimes in an transonic fan airfoil cascade", NASA TM-2002-211375, 2002.

[3] Lepicovsky, J., "Investigation of flow separation ina transonic-fan linear cascade using visualization methods", *Experiments in Fluids*, 44, 939-949, 2008.

[4] Becker, B., Reyer, M., Swoboda, M., “Steady and unsteady numerical investigation of transitional shock-boundary layer interaction on a fan blade”, *Aerospace Science and Technology*, 11, 507-517, 2007.

[5] Sanders, A.J., "Nonsynchronous vibration (NSV) due to a flow-induced aerodynamic instability in a composite fan stator", *ASME Journal of Fluids Engineering*, 127, 412–421, 2005.

[6] Chen, Li-Wei, Xu, Chang-Yue, Lu, Xi-Yun, "Numerical investigation of the compressible flow past an aerofoil", *Journal of Fluid Mechanics*, 643, 97-126, 2010.

[7] Xiong, J, Nezhad, S. T., Liu, F. "Computation of self-excited unsteady transonic flow of an Airfoil in a channel using URANS and DES", AIAA 2010-5109, 2010.

[8] Hermes, V., Klioutchnikov, I., Olivier, H., "Numerical investigation of unsteady wave phenomena for transonic airfoil flow", *Aerospace Science and Technology* (In Press), 2012. doi: 10.1016/j.ast.2012.01.009.

[9] Hasan, A. B. M. Toufique, Matsuo, S., Setoguchi, T. Kim, H.-D, and Yu, S. “Control of Transonic Flow with Non-equilibrium Condensation around a Circular Arc Blade using Bump”, *International Journal of Turbo and Jet Engines*, 26, 33-49, 2009.

[10] Raghunathan, S., Early, J.M., Tulita, C., Benard, E. , and Quest, J., "Periodic transonic flow and control", *Aeronautical Journal*, 112 , 1-16, 2008.

[11] Tijdeman H., “Investigation of the transonic flow around oscillating airfoils”, NLR Report, NLR TR-77090 U, National Aerospace Laboratory, Amsterdam, Netherlands, 1977.

[12] Tijdeman H., Seebass R., “Transonic flow past oscillating airfoils”, *Ann. Rev. Fluid Mechanics*, 12, 181-222, 1980.

[13] Gibb J., “The cause and cure of periodic flows at transonic speeds”, in: 16th Congress of the International Council of Aeronautical Science, AIAA, Washington, DC, pp. 1522–1530, 1988.

[14] McDevitt J.B., Levy L.L., Deiwert G.S., “Transonic flow about a thick circular-arc airfoil”, *AIAA Journal*, 14, 606–613, 1976.

[15] McDevitt J.B., “Supercritical Flow about a Thick Circular-Arc Airfoil”, NASA-N79-16800, 1979.

[16] Seegmiller H.L., Marvin J.G., Levy Jr. L.L., “Steady and Unsteady Transonic Flow”, *AIAA Journal*, 16, 1262-1270, 1978.

[17] Mabey D.G., Welsh B.L., Cripps B.E., “Periodic flows on a rigid 14% thick biconvex wing at transonic speeds”, RAE-TR-81059, 1981.

[18] Raghunathan S., Gillan M. A., Cooper R. X., Mitchell R.D., Cole J.S., “Shock oscillations on biconvex aerofoil’s”, *Aerospace Science and Technology*, 1, 1-9, 1999.

[19] Yamamoto K., Tanida Y., "Self-Excited Oscillation of Transonic Flow around an Airfoil in Two-Dimensional Channels", *Journal of Turbomachinery*, 112, 723-731, 1990.

[20] Lionel L., Levy Jr., "Experimental and Computational Steady and Unsteady Transonic Flows about a Thick Airfoil", *AIAA Journal*, 16, 564-572, 1978

[21] Barakos G., Drikakis D., "Numerical simulation of transonic buffet flows using various turbulence closures", *International Journal of Heat and Fluid Flow*, 21, 620-626, 2000.

[22] Xiao Q., Tsai H., Liu F., "Numerical study of transonic buffet on a supercritical airfoil", *AIAA Journal*, 44, 620–628, 2006.

[23] Deck S., "Numerical simulation of transonic buffet over a supercritical airfoil", *AIAA Journal*, 43, 1556–1566, 2005.

[24] Weber A., Schreiber H. A., Fuchs R., Steinert W., "3-D Transonic flow in a compressor cascade with shock-induced corner stall", ASME, *Journal of Turbomachinary*,124, 358–366, 2002.

[25] Weitao H., Weiyang Q., Hualing L., "Shock-wave/boundary-layer interaction in a transonic turbine cascade", Proc IMechE, Part G: *Journal of Aerospace Engineering*, 225, 77–85, 2011.

[26] Lepicovsky J., McFarland E. R., Chima R. V., Capece V. R., Hayden J., "Intermittent flow regimes in an transonic fan airfoil cascade", *International Journal of Rotating Machinery*, 10, 135–144, 2004.

[27] Bruch P. J. K., Babinsky H., "Unsteady shock wave dynamics", *Journal of Fluid Mechanics*, 603, 463-473, 2008.

[28] Gad-el-Hak , M., "Flow Control: the Future," *Journal of Aircraft*, 38, 402-418, 2001.

[29] Ashill P. R., Fulker, J. L., Hackett, K. C., “A review of recent developments in flow control”, *Journal of Aeronaut*, 105, 205-232, 2005.

[30] Menter F. R., “Two-Equation Eddy-Viscosity Turbulence Models for Engineering Applications”, *AIAA Journal*, 32, 1598-1605, 1994.

[31] Stanewsky E, Fulker J, Delery J andGeibler J., “Drag Reduction by passive Shock Control-Results of the project”, EUROSHOCK, AER2-CT92-0049, Notes on Numerical Fluid Mechanics, 56, Vieweg Verlag, 1997.

[32] Raghunthan, S., Gillan, M. A., Mitchell, R. D., “Studies on alleviation of buffet in periodic transonic flow”, *AIAA Journal*, 35, 1890-1891, 1997.

[33] Roelof V., “Governing equations in transonic flow”, Technical report, Delft University of Technology, 2008.

[34] Hasan, A.B.M. Toufique., Matsuo, S., Setoguchi, T., Islam, A.K.M. Sadrul, “Effects of condensing moist air on shock induced oscillation around an airfoil in transonic internal flows”, *Internal Journal of Mechanical Sciences*, 54, 249-259, 2012

[35] Marvin, J.G., Levy, L.L., Seegmiller, H.L, “Turbulence modeling for unsteady transonic flows”, *AIAA Journal*, 18, 489-496, 1980

[36] Lee, B.H.K., “Oscillatory shock motion caused by transonic shock boundary-layer interaction”, *AIAA Journal*, 28, 942-944, 1990

[37] Lee, B.H.K., Murty, H., Jiang, H., “Role of kutta wave on Oscillatory shock motion on an airfoil”, *AIAA Journal*, 32, 789-796, 1994